A Computational Method for Earthquake Cycles within Anisotropic Media

Maricela Best Mckay[1], Brittany A. Erickson[1], Jeremy E. Kozdon[2]
[1]Department of Mathematics and Statistics, Portland State University
[2] Department of Applied Mathematics, Naval Postgraduate School

Submitted to *Geophysical Journal International* on 28 December 2018

Abstract

We present a numerical method for the simulation of earthquake cycles on a 1D fault interface embedded in a 2D homogeneous, anisotropic elastic solid. The fault is governed by an experimentally motivated friction law known as rate-and-state friction which furnishes a set of ordinary differential equations which couple the interface to the surrounding volume. Time enters the problem through the evolution of the ODEs along the fault and provide boundary conditions for the volume, which is governed by quasi-static elasticity. We develop a time-stepping method which accounts for the interface/volume coupling, and requires solving an elliptic PDE for the volume response at each time step. The 2D volume is discretized with a second order accurate finite difference method satisfying the summation-by-parts property, with boundary and fault interface conditions enforced weakly. This framework leads to a provably stable semi-discretization. To mimic slow tectonic loading, the remote side-boundaries are displaced at a slow rate, which eventually leads to earthquake nucleation at the fault. Time stepping is based on an adaptive, fourth order Runge-Kutta method and captures the highly varying time-scales present. The method is verified with convergence tests for both the orthotropic and fully anisotropic cases. An initial parameter study reveals regions of parameter space where the systems experiences a bifurcation from period one to period two behavior. Additionally, we find that anisotropy influences the recurrence interval between earthquakes, as well as the emergence of aseismic transients and the nucleation zone size and depth of earthquakes.

1 Introduction

Modeling the full earthquake cycle poses numerous computational challenges. Interseismic periods between fault rupture last hundreds of years, punctuated by earthquakes that evolve on a time scale of seconds. The spatial scales that must be considered also encompass many orders of magnitude. Fault length is measured in kilometers while the process zone, an area directly behind the tip of a propagating rupture, must be resolved on the order of millimeters when using laboratory measured parameters (Noda, Dunham, et al., 2009). Additionally, faults in nature have nonplanar geometries, and the physical makeup of the materials that surround earthquake faults is complex and varying. Material anisotropy is present in the Earth's crust, the upper mantle, the transition zone, the D" layer, and the inner core (Long and Becker, 2010) and seismic anisotropy can be observed through shear wave splitting, that is, when a shear wave splits into two components with different propagation speeds. This splitting has been observed in most igneous, metamorphic, and sedimentary rocks in the Earth's crust (Crampin and Lovell, 1991), and is used to measure anisotropy along fault rupture zones (Cochran et al., 2003). While seismic anisotropy is present in the real world, many cycle models make the simplifying assumption of isotropic material properties (Lapusta, Rice, et al., 2000; Erickson and Dunham, 2014; Allison and Dunham, 2018).

Methods currently used for simulating earthquake cycles can generally be broken into two broad categories: spectral boundary integral techniques, and numerical discretizations of off-fault volumes like finite difference and finite element methods. Hajarolasvadi and Elbanna (2017) detail the benefits and drawbacks of spectral boundary integral methods, namely, that they are computationally efficient (as they reduce 2D problems to 1D and 3D problems to 2D (Geubelle and Rice, 1995; Cochard and Madariaga, 1994)) and require no artificial truncation of the computational domain. However, these methods are currently limited to the simplifying assumption that the Earth's material properties are homogeneous, isotropic and linear elastic. This motivates the use of volume-based numerical methods, such as finite element and finite difference methods which can account for material anisotropy, heterogeneity, and off-fault plasticity (Kaneko et al., 2008; Erickson and Dunham, 2014; Erickson, Dunham, and Khosravifar, 2017; Allison and Dunham, 2018).

In this work, where our focus is on anisotropic material properties, we elect to use a finite difference formulation satisfying a summation-by-parts (SBP) rule, with weak enforcement of boundary conditions through the simultaneous-approximation-term (SAT), which have the desirable property that the discretization is provably energy stable. This computational framework is an extension of that of Erickson and Dunham (2014) to incorporate material anisotropy. Our main focus is a parameter exploration of the homogeneous, anisotropic problem. The paper is organized as follows: In section 2 we define the governing equation and constitutive relations for an anisotropic elastic material. In section 3 we provide details of the spatial discretization and derive conditions that render the semi-discrete equations stable. In section 4 we provide details of the frictional fault that forms one boundary of the domain and describe the adaptive Runge-Kutta based time-stepping method. Section 5 is a linear stability analysis of frictional sliding for the anisotropic problem that extends the analysis done in Ranjith and Gao (2007). To verify our computational strategy, we perform convergence tests in section 6 and confirm that our numerical solution is converging at the expected rate. Results from our parameter varying study are detailed in section 7.

2 Governing Equations

We consider a vertical, strike-slip fault embedded in a 2D volume given by $(y, z) \in (-L_y, L_y) \times (0, L_z)$. We assume that the only non-zero component of displacement, denoted as u, occurs in the x-direction and that motion is invariant in this direction, so that $u = u(t, y, z)$. The fault, at $y = 0$, serves as a frictional interface embedded in an anisotropic, homogeneous material. Across the fault interface the components of traction are taken to be equal in magnitude but opposite in sign and the displacement u is allowed to have a jump. The jumps in displacement are governed by a friction law which couples the volume solution to a set of local auxiliary state variables governed by an ODE; the details of the frictional framework are given in Section 4.

Since the domain is symmetric about the fault and the material properties are homogeneous, the solution across the fault will be anti-symmetric. Exploiting this symmetry allows us to consider the one sided domain $(y, z) \in \Omega = (0, L_y) \times (0, L_z)$. In this setting, the anisotropic elastic wave equation is

$$\rho \frac{\partial^2 u}{\partial t^2} = \frac{\partial}{\partial y}\left[\mu_1 \frac{\partial u}{\partial y} + \mu_2 \frac{\partial u}{\partial z}\right] + \frac{\partial}{\partial z}\left[\mu_2 \frac{\partial u}{\partial y} + \mu_3 \frac{\partial u}{\partial z}\right], \qquad (y, z) \in \Omega, \tag{1}$$

where ρ is the material density and μ_1, μ_2 and μ_3; we assume that the elastic moduli satisfy $\mu_1 > 0$, $\mu_3 > 0$, and $\mu_1\mu_3 > \mu_2^2$. Using Hooke's law, the relevant components of traction that will be needed later are:

$$\sigma_{xy}(t, y, z) = \mu_1 \frac{\partial u}{\partial y} + \mu_2 \frac{\partial u}{\partial z} \tag{2a}$$

$$\sigma_{xz}(t, y, z) = \mu_2 \frac{\partial u}{\partial y} + \mu_3 \frac{\partial u}{\partial z}. \tag{2b}$$

We impose the following boundary conditions on $\partial\Omega$:

$$u(t, 0, z) = g_L(t, z), \tag{3a}$$

$$u(t, L_y, z) = g_R(t, z), \tag{3b}$$

$$\sigma_{xz}(t, y, 0) = 0, \tag{3c}$$

$$\sigma_{xz}(t, y, L_z) = 0. \tag{3d}$$

Condition (3c) corresponds to the Earth's free surface and condition (3d) the assumption that the material below depth L_z exerts no traction on the overlying material. The displacement boundary condition data $g_L(t, z)$ is determined by the friction law and $g_R(t, z)$ imposes the remote tectonic loading; see Section 4. In order to derive parameters in the discretization, in Equation (1) we have retained the inertial term $\partial^2 u/\partial t^2$. Later, in order to make the problem more computationally tractable, this inertial term will be replaced with the radiation damping approximation (Rice, 1993) which will result in a modifications to boundary condition (3a).

Energy-boundedness of the Solution: To ensure that the initial boundary value problem (1)-(3) is well-posed we use the energy method. We assume homogeneous boundary conditions, with the understanding that the analysis for zero boundary data can be extended to non-homogeneous boundary conditions via Duhamel's principal. Letting $||\cdot||$ denote the L^2 norm, multiplying (1) by $\dfrac{\partial u}{\partial t}$, integrating over Ω and applying Green's theorem on the right-hand side yields:

$$\frac{1}{2}\frac{\partial}{\partial t}\left\|\rho \frac{\partial u}{\partial t}\right\|^2 = B_r + B_s + B_d + B_f - \frac{1}{2}\frac{\partial}{\partial t}\int_0^{L_y}\!\!\int_0^{L_z} \begin{bmatrix} \frac{\partial u}{\partial y} & \frac{\partial u}{\partial z} \end{bmatrix} \begin{bmatrix} \mu_1 & \mu_2 \\ \mu_2 & \mu_3 \end{bmatrix} \begin{bmatrix} \frac{\partial u}{\partial y} \\ \frac{\partial u}{\partial z} \end{bmatrix} dz\, dy, \tag{4}$$

where the boundary terms are given by

$$B_r = \int_0^{L_z} \left(\mu_1 \frac{\partial u}{\partial t}\frac{\partial u}{\partial y} + \mu_2 \frac{\partial u}{\partial t}\frac{\partial u}{\partial z} \right) \Big|_{y=L_y} dz = \int_0^{L_z} \left(\frac{\partial u}{\partial t} \sigma_{xy}(t,y,z) \right) \Big|_{y=L_y} dz, \tag{5a}$$

$$B_f = -\int_0^{L_z} \left(\mu_1 \frac{\partial u}{\partial t}\frac{\partial u}{\partial y} + \mu_2 \frac{\partial u}{\partial t}\frac{\partial u}{\partial z} \right) \Big|_{y=0} dz = \int_0^{L_z} \left(\frac{\partial u}{\partial t} \sigma_{xy}(t,y,z) \right) \Big|_{y=0} dz, \tag{5b}$$

$$B_d = \int_0^{L_y} \left(\mu_2 \frac{\partial u}{\partial t}\frac{\partial u}{\partial z} + \int_0^{L_y} \mu_3 \frac{\partial u}{\partial t}\frac{\partial u}{\partial z} \right) \Big|_{z=L_z} dy = \int_0^{L_z} \left(\frac{\partial u}{\partial t} \sigma_{xz}(t,y,z) \right) \Big|_{z=L_z} dy, \tag{5c}$$

$$B_s = -\int_0^{L_y} \left(\mu_2 \frac{\partial u}{\partial t}\frac{\partial u}{\partial z} + \int_0^{L_y} \mu_3 \frac{\partial u}{\partial t}\frac{\partial u}{\partial z} \right) \Big|_{z=0} dy = \int_0^{L_z} \left(\frac{\partial u}{\partial t} \sigma_{xy}(t,y,z) \right) \Big|_{z=0} dy. \tag{5d}$$

Letting $\mathbf{U} = [u_1 \quad u_2]^T$ allows us to define the norm

$$\|\mathbf{U}\|^2_{M_\mu} = \int_0^{L_z}\!\!\int_0^{L_y} \mathbf{U}^T \mathbf{M}_\mu \mathbf{U} \, dy \, dz, \quad \mathbf{M}_\mu = \begin{bmatrix} \mu_1 & \mu_2 \\ \mu_2 & \mu_3 \end{bmatrix}. \tag{6}$$

Here, $\mathbf{M}_\mu$ is symmetric positive-definite due to the restrictions on the shear moduli given after Equation (1). The energy method is now complete, since we can write (4) as

$$\frac{1}{2}\frac{\partial}{\partial t} \left(\left\| \sqrt{\rho} \frac{\partial u}{\partial t} \right\|^2 + \left\| \begin{bmatrix} \frac{\partial u}{\partial y} & \frac{\partial u}{\partial z} \end{bmatrix}^T \right\|^2_{M_\mu} \right) = B_r + B_s + B_d + B_f, \tag{7}$$

where the terms on the left of (7) correspond to the rate of change of kinetic and strain energy, respectively, and the terms on the right represent rate of work done on the elastic body by tractions on the boundaries. For zero boundary data, B_r, B_s, B_d, and B_f vanish, and energy is conserved.

3 Spatial Discretization

Our aim is to discretize (1) and (3) in a provably stable and accurate way, with a semi-discrete estimate that mimics (7). To do this we will use finite difference approximations satisfying a summation-by-parts (SBP) rule with boundary and interface conditions enforced weakly using the simultaneous approximation term (SAT) method (Kreiss and Scherer, 1974; Kreiss and Scherer, 1977; Strand, 1994; Mattsson and Nordström, 2004). We begin by describing the 1D SBP operators and then move on to the Kronecker product construction of the 2D operators. We conclude the section by describing the full 2D discretization of (1) and (3) and then stating a previously derived stability result.

Consider the 1D domain $\Omega_y = [0, L_y]$ discretized into an evenly spaced grid of $N_y + 1$ points. We let the grid points be $y_j = j \; h_y$ for $j = 0, 1, \dots, N_y$ with spacing $h_y = L_y/N_y$. We let grid function $\mathbf{p}^T = [p_0, \dots, p_{N_y}]$ be the interpolation of function p with $p_j = p(y_j)$. The first derivative of p is approximated as:

$$\frac{\partial p}{\partial y} \approx \mathbf{D}_1 \mathbf{p} = \mathbf{H}^{-1} \mathbf{Q} \mathbf{p}. \tag{8}$$

Here the finite difference matrix $\mathbf{D}_1$ is of size $(N_y + 1) \times (N_y + 1)$. The matrix $\mathbf{H}$ is diagonal and positive and can be thought of as a numerical quadrature rule (Hicken and Zingg, 2013), namely

$$\int_0^{L_y} pq \, dy \approx \mathbf{p}^T \mathbf{H} \mathbf{q}. \tag{9}$$

The matrix $\mathbf{Q}$ is an almost skew symmetric matrix with the property that

$$\mathbf{Q} + \mathbf{Q}^T = \mathbf{B} = \mathrm{diag}[-1,\ 0,\ 0\ \ldots,\ 0,\ 1]. \tag{10}$$

Operators with this structure are called SBP due to the identity

$$\mathbf{q}^T \mathbf{H} \mathbf{D}_1 \mathbf{p} = \mathbf{q}^T \mathbf{Q} \mathbf{p} = \mathbf{q}^T \left(\mathbf{B} - \mathbf{Q}^T \right) \mathbf{p} = q_{N_y} p_{N_y} - q_0 p_0 - \mathbf{q}^T \mathbf{D}_1^T \mathbf{H} \mathbf{p}, \tag{11}$$

which discretely mimics integration by parts,

$$\int_0^{L_y} q \frac{\partial p}{\partial y} \, dy = q\left(L_y\right) p\left(L_y\right) - q\left(0\right) p\left(0\right) - \int_0^{L_y} \frac{\partial q}{\partial y} p \, dy. \tag{12}$$

One approach to defining a second derivative operator is to apply $\mathbf{D}_1$ twice:

$$\frac{\partial^2 p}{\partial y^2} \approx \mathbf{D}_1 \mathbf{D}_1 \mathbf{p}. \tag{13}$$

One downside of this is that it increases the bandwidth of the operator. Thus we instead prefer to use the compact SBP second derivative operators of Mattsson and Nordström (2004):

$$\frac{\partial^2 p}{\partial y^2} \approx \mathbf{D}_2 \mathbf{p} = \mathbf{H}^{-1} \left(-\mathbf{M} + \mathbf{B} \mathbf{S} \right) \mathbf{p}. \tag{14}$$

The matrix $\mathbf{M}$ is symmetric positive definite, and can be thought of as approximating the inner product of derivatives:

$$\int_0^{L_y} \frac{\partial p}{\partial y} \frac{\partial q}{\partial y} \, dy \approx \mathbf{p}^T \mathbf{M} \mathbf{q}. \tag{15}$$

Matrix $\mathbf{B}$ is as defined above and $\mathbf{S}$ is an approximation of the first derivative; note that in general $\mathbf{S} \neq \mathbf{D}_1$. We assume that $\mathbf{H}$ in Equations (8) and (14) are the same, namely the operators are compatible. Operator $\mathbf{D}_2$ is called SBP since

$$\mathbf{p}^T \mathbf{H} \mathbf{D}_2 \mathbf{q} = \mathbf{p}_{N_y} \left(\mathbf{S}\right)_{N_y} - \mathbf{p}_0 \left(\mathbf{S}\right)_0 - \mathbf{p}^T \mathbf{M} \mathbf{q}, \tag{16}$$

discretely mimics the continuous identity

$$\int_0^{L_y} p \frac{\partial^2 q}{\partial y^2} \, dy = p\left(L_y\right) \left. \frac{\partial q}{\partial y} \right|_{y=L_y} - p\left(0\right) \left. \frac{\partial q}{\partial y} \right|_{y=0} - \int_0^{L_y} \frac{\partial p}{\partial y} \frac{\partial q}{\partial y} \, dy. \tag{17}$$

In this work we will exclusively consider the second order accurate SBP operators, which are central difference operators in the interior and one-sided at the boundary. Note that the operators are second order accurate in the interior but only first order accurate at the boundary;

however the global accuracy of these operator is 2 (Gustafsson, 1975; Strand, 1994; Mattsson and Nordström, 2004). The operators we use are:

$$
\mathbf{D}_1 = \frac{1}{h_y}\begin{bmatrix} -1 & 1 & & & & \\ -\frac{1}{2} & 0 & \frac{1}{2} & & & \\ & -\frac{1}{2} & 0 & \frac{1}{2} & & \\ & & \ddots & \ddots & \ddots & \\ & & & -\frac{1}{2} & 0 & \frac{1}{2} \\ & & & & -1 & 1 \end{bmatrix}, \quad \mathbf{D}_2 = \frac{1}{h_y^2}\begin{bmatrix} 1 & -2 & 1 & & & \\ 1 & -2 & 1 & & & \\ & 1 & -2 & 1 & & \\ & & \ddots & \ddots & \ddots & \\ & & & 1 & -2 & 1 \\ & & & 1 & -2 & 1 \end{bmatrix}, \tag{18}
$$

where the SBP factors of the operators are

$$
\mathbf{H} = \mathrm{diag}\left[\frac{1}{2},\ 1,\ 1\ \ldots,\ 1,\ \frac{1}{2}\right], \qquad \mathbf{Q} = \begin{bmatrix} -\frac{1}{2} & \frac{1}{2} & & & \\ -\frac{1}{2} & 0 & \frac{1}{2} & & \\ & \ddots & \ddots & \ddots & \\ & & -\frac{1}{2} & 0 & \frac{1}{2} \\ & & & -\frac{1}{2} & \frac{1}{2} \end{bmatrix}, \tag{19}
$$

$$
\mathbf{S} = \begin{bmatrix} -\frac{3}{2} & 2 & -\frac{1}{2} & & \\ & 1 & & & \\ & & \ddots & & \\ & & & 1 & \\ & & \frac{1}{2} & -2 & \frac{3}{2} \end{bmatrix}, \qquad \mathbf{M} = \begin{bmatrix} 1 & -1 & & & \\ -1 & 2 & -1 & & \\ & \ddots & \ddots & \ddots & \\ & & -1 & 2 & -1 \\ & & & -1 & 1 \end{bmatrix}. \tag{20}
$$

The 1D operators can be extended to multiple dimensions via the Kronecker product. The Kronecker product of matrices $\mathbf{A}$ and $\mathbf{C}$ is defined as

$$
\mathbf{A} \otimes \mathbf{C} = \begin{bmatrix} a_{0,0}\mathbf{C} & \ldots & a_{0,m}\mathbf{C} \\ \vdots & \ddots & \vdots \\ a_{m,0}\mathbf{C} & \ldots & a_{m,n}\mathbf{C} \end{bmatrix}
$$

where $\mathbf{A}$ is of size $m \times n$, $\mathbf{C}$ is of size $l \times k$, and $\mathbf{A} \otimes \mathbf{C}$ is of size $ml \times nk$. We define the grid function of p as

$$
\bar{\mathbf{p}} = [\mathbf{p}_0^T, \mathbf{p}_1^T, \ldots \mathbf{p}_{N_y}^T]^T \tag{21}
$$

with $\mathbf{p}_i = [p_{i,0}, p_{i,1}, \ldots p_{i,N_z}]^T$ for $i = 0, \ldots N_y$ and $p_{i,j} \approx p(y_i, z_j)$. The derivative approximations are then:

$$
\frac{\partial p}{\partial y} \approx \left(\mathbf{D}_1^{(y)} \otimes \mathbf{I}^{(z)}\right)\bar{\mathbf{p}} = \bar{\mathbf{D}}_1^{(y)}\bar{\mathbf{p}}, \qquad \frac{\partial p}{\partial z} \approx \left(\mathbf{I}^{(y)} \otimes \mathbf{D}_1^{(z)}\right)\bar{\mathbf{p}} = \bar{\mathbf{D}}_1^{(z)}\bar{\mathbf{p}}, \tag{22a}
$$

$$
\frac{\partial^2 p}{\partial y^2} \approx \left(\mathbf{D}_2^{(y)} \otimes \mathbf{I}^{(z)}\right)\bar{\mathbf{p}} = \bar{\mathbf{D}}_2^{(y)}\bar{\mathbf{p}}, \qquad \frac{\partial^2 p}{\partial z^2} \approx \left(\mathbf{I}^{(y)} \otimes \mathbf{D}_2^{(z)}\right)\bar{\mathbf{p}} = \bar{\mathbf{D}}_2^{(z)}\bar{\mathbf{p}}. \tag{22b}
$$

Here $\mathbf{I}^{(y)}$ and $\mathbf{I}^{(z)}$ are identity matrices of size $(N_y+1) \times (N_y+1)$ and $(N_z+1) \times (N_z+1)$; the superscripts (y) and (z) in the derivative matrix indicate whether the operator is for the y or z dimensions, respectively.

With the above notation in place, we can now define the semidiscrete version of (1) and (3) as (Virta and Mattsson, 2014)

$$
\rho\frac{d^2\bar{\mathbf{u}}}{dt^2} = \mu_1\bar{\mathbf{D}}_2^{(y)}\bar{\mathbf{u}} + \mu_2\bar{\mathbf{D}}_1^{(y)}\bar{\mathbf{D}}_1^{(z)}\bar{\mathbf{u}} + \mu_2\bar{\mathbf{D}}_1^{(z)}\bar{\mathbf{D}}_1^{(y)}\bar{\mathbf{u}} + \mu_3\bar{\mathbf{D}}_2^{(z)}\bar{\mathbf{u}} + \bar{\mathbf{p}}_L + \bar{\mathbf{p}}_R + \bar{\mathbf{p}}_B + \bar{\mathbf{p}}_T. \tag{23}
$$

Here, the vectors $\bar{\mathbf{p}}_L$, $\bar{\mathbf{p}}_R$, $\bar{\mathbf{p}}_B$, and $\bar{\mathbf{p}}_T$ are penalty vectors that enforce the boundary and interface conditions. These vectors are defined as

$$\left(\mathbf{H}^{(y)} \otimes \mathbf{H}^{(z)}\right) \bar{\mathbf{p}}_L = \left(\alpha \left(\mathbf{I}^{(y)} \otimes \mathbf{H}^{(z)}\right) - \left(\mu_1 \bar{\mathbf{S}}^{(y)} + \mu_2 \bar{\mathbf{D}}^{(z)}\right)^T \left(\mathbf{I}^{(y)} \otimes \mathbf{H}^{(z)}\right)\right) \bar{\mathbf{E}}_L \left(\bar{\mathbf{u}} - \bar{\mathbf{g}}_L\right), \tag{24a}$$

$$\left(\mathbf{H}^{(y)} \otimes \mathbf{H}^{(z)}\right) \bar{\mathbf{p}}_R = \left(\alpha \left(\mathbf{I}^{(y)} \otimes \mathbf{H}^{(z)}\right) + \left(\mu_1 \bar{\mathbf{S}}^{(y)} + \mu_2 \bar{\mathbf{D}}^{(z)}\right)^T \left(\mathbf{I}^{(y)} \otimes \mathbf{H}^{(z)}\right)\right) \bar{\mathbf{E}}_R \left(\bar{\mathbf{u}} - \bar{\mathbf{g}}_R\right), \tag{24b}$$

$$\left(\mathbf{H}^{(y)} \otimes \mathbf{H}^{(z)}\right) \bar{\mathbf{p}}_B = \left(\mathbf{H}^{(y)} \otimes \mathbf{I}^{(z)}\right) \bar{\mathbf{E}}_B \left(\mu_2 \bar{\mathbf{D}}^{(y)} + \mu_3 \bar{\mathbf{S}}^{(z)}\right) \bar{\mathbf{u}}, \tag{24c}$$

$$\left(\mathbf{H}^{(y)} \otimes \mathbf{H}^{(z)}\right) \bar{\mathbf{p}}_T = -\left(\mathbf{H}^{(y)} \otimes \mathbf{I}^{(z)}\right) \bar{\mathbf{E}}_T \left(\mu_2 \bar{\mathbf{D}}^{(y)} + \mu_3 \bar{\mathbf{S}}^{(z)}\right) \bar{\mathbf{u}}. \tag{24d}$$

Here the vectors $\bar{\mathbf{g}}_L$ and $\bar{\mathbf{g}}_R$ are the grid functions which are zero everywhere except for along the left and right boundaries where they take the values of g_L and g_R, respectively (see (3)). The matrices $\bar{\mathbf{E}}_L$, $\bar{\mathbf{E}}_R$, $\bar{\mathbf{E}}_B$, and $\bar{\mathbf{E}}_T$ zero out all values in a vector except those along the left, right, bottom, and top boundaries, respectively, and are defined as

$$\bar{\mathbf{E}}_L = \operatorname{diag}(1,\ 0,\ \ldots,\ 0) \otimes \mathbf{I}^{(z)}, \qquad \bar{\mathbf{E}}_R = \operatorname{diag}(0,\ \ldots,\ 0,\ 1) \otimes \mathbf{I}^{(z)}, \tag{25a}$$

$$\bar{\mathbf{E}}_B = \mathbf{I}^{(y)} \otimes \operatorname{diag}(0,\ \ldots,\ 0,\ 1), \qquad \bar{\mathbf{E}}_T = \mathbf{I}^{(y)} \otimes \operatorname{diag}(1,\ 0,\ \ldots,\ 0). \tag{25b}$$

The 2D boundary derivative matrices are

$$\bar{\mathbf{S}}^{(y)} = \mathbf{S}^{(y)} \otimes \mathbf{I}^{(z)}, \qquad \bar{\mathbf{S}}^{(z)} = \mathbf{S}^{(z)} \otimes \mathbf{I}^{(z)}. \tag{26a}$$

Penalty terms $\bar{\mathbf{p}}_B$ and $\bar{\mathbf{p}}_T$ enforce the free surface boundary conditions whereas $\bar{\mathbf{p}}_L$ and $\bar{\mathbf{p}}_R$ enforce the Dirchlet boundary and fault interface conditions (hence the need to subtract off data from the solution vector). The scalar parameter α in $\bar{\mathbf{p}}_L$ and $\bar{\mathbf{p}}_R$ needs to be sufficiently large (in magnitude) so that the discretization is energy stable. For the second order accurate operators used here, the results of Virta and Mattsson (2014) (reduced to the case of constant coefficients) show that α must satisfy

$$\alpha \le -\frac{99}{36}\frac{\mu_1^2}{\lambda h_y} - \frac{2\mu_3^2}{\lambda h_y}, \quad \lambda = \tfrac{1}{2}(\mu_1 + \mu_3) - \sqrt{(\mu_1 - \mu_3)^2 + 4\mu_2^2}. \tag{27}$$

With zero boundary data, $g_L = g_R = 0$, Virta and Mattsson (2014) derive an energy estimate for the numerical solution to the semi-discrete equations, showing the scheme is energy stable.

4 Frictional Framework

The displacements and tractions on the two sides of a fault interface, located at $y = 0$ in our model, are related to one another via a nonlinear friction law that enforces continuity of traction while allowing for a jump in displacement. We define the slip velocity, or the time derivative of the jump in displacement across the fault by

$$V(z,t) = \frac{\partial \Delta u(z,t)}{\partial t}, \tag{28a}$$

$$\Delta u(z,t) = \lim_{\epsilon \to 0^+} \left(u(\epsilon, z, t) - u(-\epsilon, z, t)\right), \tag{28b}$$

and the shear stress on the fault by

$$\tau = \sigma_{xy}(0, z, t) = \left(\mu_1 \frac{\partial u}{\partial y} + \mu_2 \frac{\partial u}{\partial z}\right)\Big|_{y=0}, \tag{29}$$

i.e., the component of traction in the x-direction, on the $y \leq 0$ side of the interface, that comes from the $y \geq 0$ side. Rate-and-state friction relates the shear stress τ on the fault to a nonlinear function of the slip velocity V and a state variable Ψ which obeys a local ordinary differential equation that tracks the history of sliding (Dieterich, 1979; Marone, 1998):

$$\tau = F(V, \Psi), \tag{30a}$$

$$\frac{d\Psi}{dt} = G(V, \Psi). \tag{30b}$$

These relationships along with continuity of traction, i.e., $\Delta\sigma_{xy} = 0$ across the fault, fully specify the problem. The specific forms of F and G we use are:

$$F(V, \Psi) = a\sigma_n \sinh^{-1}\left(\frac{V}{2V_0} e^{\frac{\Psi}{a}}\right), \tag{31a}$$

$$G(V, \Psi) = \frac{bV_0}{D_c}\left(e^{\frac{f_0 - \Psi}{b}} - \frac{V}{V_0}\right), \tag{31b}$$

where f_0 is a reference friction coefficient for steady sliding at slip velocity V_0, a and b are dimensionless parameters characterizing the direct and state evolution effects, respectively, σ_n is the effective normal stress on the fault, and D_c is the state evolution distance.

An important feature of the friction law is that even though the governing equations are linear in the volume, friction law (31a) is nonlinear. This nonlinearity poses no computational challenge if explicit time integration is used for semi-discretization (23), as the friction law only enters on the right-hand side of the equation; see for instance Kozdon et al. (2012). The problem with using explicit time integration for earthquake cycle simulations is that the CFL restriction will lead to a very small time step (on the order of milliseconds with realistic material parameters) which would make long time simulations (hundreds of years) impractical. One approach would be to use implicit time stepping when the slip velocity V along the whole fault is low to thus “step over” the extremly low frequency waves. The problem with this approach is that the friction law (31a) then leads to a large nonlinear system of equations that must be solved. Thus here, following Erickson and Dunham (2014), we set the inertial term $d^2\bar{\mathbf{u}}/dt^2$ in the semi-discretization (23) to zero. With this semi-discretization (23) then becomes a linear system of the form:

$$\bar{\mathbf{A}}\bar{\mathbf{u}} = \bar{\mathbf{b}}(\boldsymbol{\Delta}\mathbf{u}, t). \tag{32}$$

Here $\bar{\mathbf{A}}$ is a matrix of size $N_p \times N_p$ and $\bar{\mathbf{b}}(\boldsymbol{\Delta}\mathbf{u}, t)$ is a vector of size N_p where in both cases $N_p = (N_y + 1)(N_z + 1)$ is the total number of grid points. The vector $\bar{\mathbf{b}}(\boldsymbol{\Delta}\mathbf{u}, t)$ incorporates the boundary conditions, which due to the friction law and outer boundary depend on both t and Δu. Note that in semi-discretization (23), symmetry implies that $g_L = \Delta u/2$, namely the jump in displacement on the fault is accommodated equally on both sides.

By zeroing out the inertial terms we are then saying that changes in displacement on the fault (and outer boundary) instantaneously modify displacements in the interior. This assumption is valid when the magnitude of the slip velocity is low, $|V| \ll 1$, but for higher sliding velocities waves must be approximated in some way for the problem to remain relevant and well-posed. Here we use the radiation damping approximation (Rice, 1993). In this approach waves that result from slip on the fault are assumed to emit shear waves that propagate normal to the fault. The effect of this is that shear stress on the fault is decreased by a factor of ηV

where $\eta = \sqrt{\mu_1 \rho}/2$ is half the shear-wave impedance. With this, the friction law is modified to:

$$\tau_{qs} - \eta V = F(V, \Psi), \tag{33}$$

where τ_{qs} is the "quasi-static" shear stress (computed via (29)), based on the solving (23) without inertial terms.

In this formulation, time enters the equation through the state evolution equation (30b) and when Δu is updated using (28a). Given a value of Δu and Ψ all that remains to be determined is V (since G can be evaluated once V and Ψ are known). To determine $\mathbf{V}$ the following approach is used at a time t given $\mathbf{\Delta u}$ and $\mathbf{\Psi}$ (here we use vector notation to denote that these quantities are grid function along the fault).

1. The linear system (32) is solved for $\bar{\mathbf{u}}$
2. The displacement vector $\bar{\mathbf{u}}$ is then used to compute τ as

$$\boldsymbol{\tau}_{qs} = \left([1\ 0\ \ldots\ 0] \otimes \mathbf{I}^{(z)}\right)\left(\mu_1 \bar{\mathbf{S}}^{(y)} \bar{\mathbf{u}} + \mu_2 \bar{\mathbf{D}}^{(z)}\right) \tag{34}$$

3. At each grid point along the fault the nonlinear system

$$[\tau_{qs}]_i - \eta V_i = F\left(V_i, \Psi_i\right), \tag{35}$$

   is solved for V_i. Here V_i, $[\tau_{qs}]_i$, and Ψ_i are the values of these variables at each of the grids points with $i = 0,\ 1,\ \ldots,\ N_z$.

The ODEs are then integrated in time using an adaptive time step Runge-Kutta method.

5 Determination of Maximum Stable Grid Spacing: Linear Stability Analysis of Frictional Sliding

One of the important considerations in fracture modeling, such as earthquake cycle simulations, is the determination of the maximum stable grid spacing required (along the fault) so that numerical errors do not trigger unstable slip. That is, a well-posed fracture mechanics problem will have some critical wavelength h^* such that perturbations which have wavelengths h^* will decay in time whereas perturbations with wavelength greater than h^* will grow (leading to unstable sliding). The implication for grid spacing in a finite difference method is that h^* must be resolved with at least a few grid points so that the smallest wavelength discrete solutions decay; there is an additional length-scale, known as cohesive, or process zone size, that must also be resolved and this is discussed at the end of this section.

In order to determine h^* we extend the linear stability analysis of Ranjith and Gao (2007) to the anisotropic case. We consider antiplane sliding of two identical anisotropic elastic half-spaces separated by a frictional fault at $y = 0$.

We Laplace transform the equilibrium version of Equation (1) in time to obtain

$$0 = \mu_1 \frac{\partial^2 \hat{u}}{\partial y^2} + 2\mu_2 \frac{\partial^2 \hat{u}}{\partial y \partial z} + \mu_3 \frac{\partial^2 \hat{u}}{\partial z^2}. \tag{36}$$

Letting the solution to Equation (36) be of the form

$$\hat{u}(y, z, p) = \hat{\mathcal{U}}(y, k, p) e^{ikz}, \tag{37}$$

where p is the Laplace transformed variable, we then get

$$0 = \mu_1 \frac{\partial^2 \hat{\mathcal{U}}}{\partial y^2} + 2ik\mu_2 \frac{\partial \hat{\mathcal{U}}}{\partial y} + (ik)^2 \mu_3 \hat{\mathcal{U}}. \tag{38}$$

Solutions of the ordinary differential equation (38) are of the form

$$\hat{\mathcal{U}}(y,k,p) = \begin{cases} \hat{\mathcal{U}}^{(+)}(k,p) e^{\alpha^{(+)} y}, & y > 0, \\ \hat{\mathcal{U}}^{(-)}(k,p) e^{\alpha^{(-)} y}, & y < 0. \end{cases} \tag{39}$$

Here we have used the superscript $(+)$ to denote the positive side of the fault ($y > 0$), and $(-)$ to denote the side $y < 0$. The characteristic roots $\alpha^{(\pm)}$ are found by substituting in solution (39) into ordinary differential equation (38) and solving the resulting quadratic equation:

$$\alpha^{(\pm)} = \frac{-ik\mu_2 \mp \sqrt{k^2 (\mu^*)^2}}{\mu_1}, \quad \mu^* = \sqrt{\det \begin{bmatrix} \mu_1 & \mu_2 \\ \mu_2 & \mu_3 \end{bmatrix}}; \tag{40}$$

here we have chosen the root on each side of the fault so that $\alpha^{(\pm)} y$ has a negative real part and the thus the solution decays as $|y| \to \infty$. Putting this all together then yields

$$\hat{u}(y,z,p) = \begin{cases} \hat{\mathcal{U}}^{(+)}(k,p) e^{\alpha^{(+)} y + ikz}, & y > 0, \\ \hat{\mathcal{U}}^{(+)}(k,p) e^{\alpha^{(-)} y + ikz}, & y < 0, \end{cases} \tag{41}$$

or upon transforming back from Laplace space

$$u(y,z,t) = \begin{cases} \mathcal{U}^{(+)}(k,t) e^{\alpha^{(+)} y + ikz}, & y > 0, \\ \mathcal{U}^{(+)}(k,t) e^{\alpha^{(-)} y + ikz}, & y < 0. \end{cases} \tag{42}$$

The Laplace transform of traction on the two sides of the fault at $y = 0$ is

$$\hat{\sigma}_{xz}^{(\pm)} = \hat{T}^{(\pm)} e^{ikz}, \quad \hat{T}^{(\pm)} = \left(\mu_1 \alpha^{(\pm)} + ik\mu_2\right) \mathcal{U}^{\hat{(\pm)}}(k,t). \tag{43}$$

Continuity of traction implies that $\hat{T}^{(+)} = \hat{T}^{(-)}$, which after some simplification gives

$$-|k|\mu^* \hat{\mathcal{U}}^{(+)}(k,p) = |k|\mu^* \hat{\mathcal{U}}^{(-)}(k,p). \tag{44}$$

The jump in displacement across the fault is

$$\hat{u}(0^+,z,p) - \hat{u}(0^-,z,p) = \hat{D}(k,p) e^{ikz}, \quad \hat{D}(k,p) = \hat{\mathcal{U}}^{(+)}(k,p) - \hat{\mathcal{U}}^{(-)}(k,p). \tag{45}$$

Using $\hat{D}$ along with continuity of traction allows us then to relate slip to traction:

$$\hat{T}(k,p) = \frac{\hat{T}^{(+)}(k,p) + \hat{T}^{(-)}(k,p)}{2} = -\frac{|k|}{2} \mu^* \hat{D}(k,p). \tag{46}$$

Laplace transforming of the time derivative of the linearized rate-and-state friction law is (Ranjith and Gao, 2007)

$$\left(p + \frac{V_0}{D_c}\right) \hat{T} = \frac{\sigma_n}{V_0} \left(ap - (b-a)\frac{V_0}{D_c}\right) p\hat{D}. \tag{47}$$

Substitution of (46) into (47) yields the quadratic

$$\frac{\sigma_n}{V_0} ap^2 + p\left(\frac{|k|}{2}\mu^* - \frac{(b-a)\sigma_n}{D_c}\right) + \frac{V_0}{D_c}\frac{|k|}{2}\mu^* = 0. \tag{48}$$

The system will undergo Hopf bifurcation when roots p cross the imaginary axis, which will occur when $|k|$ is less than the critical wave number k_{cr}:

$$|k_{cr}| = \frac{2(b-a)\sigma_n}{D_c \mu^*}. \tag{49}$$

In terms of wavelength, this corresponds to the critical wavelength

$$h^* = \frac{2\pi}{|k_{cr}|} = \frac{\pi \mu^* D_c}{(b-a)\sigma_n}. \tag{50}$$

This then implies that we want our grid spacing to be smaller than h^* so that numerical noise does not trigger ruptures.

As noted above, Ampuero and Rubin (2008) derive an even smaller length scale called the cohesive zone, which, for the anisotropic problem we interpret to be

$$L_b = \frac{\mu^* D_c}{\sigma_n b}. \tag{51}$$

The cohesive zone length L_b corresponds to the spatial length scale over which the shear stress drops from its peak to residual values at the propagating rupture front; numerical studies of quasidynamic earthquake cycle simulations in isotropic materials observe that L_b must be resolved with at least one grid point (Ampuero and Rubin, 2008). In our simulations we resolve L_b with at least 5 grid points. To ensure that this grid spacing is sufficient, we doubled the number of grid points so that L_b and h^* were resolved with over 10 and 120 grid points respectively. Comparison to simulations with doubled resolution indicates that resolving L_b with over 5 grid points is adequate; see Appendix A.

6 Convergence Tests

We verify our numerical method via the method of manufactured solutions (Roache, 1998). In this approach source terms are added to (1) and (3) so that a known function can be used as an analytic solution. Namely, we let the exact displacement $\hat{u}$ be given as:

$$\hat{u}(t,y,z) = \frac{\delta}{2}K(t)\phi(y,z) + \frac{V_p t}{2}\left(1-\phi(y,z)\right) + \frac{\tau^\infty}{\mu_1}y, \tag{52}$$

where $K(t)$ and $\phi(y,z)$ are functions which will determine the temporal and spatial dependence of the solution. These functions will be chosen so that the solution exhbitis both an interseismic (slow) and coseismic (fast) phase. Namely, there will be an initial interseismic phase, followed by a single coseismic phase, and another interseismic phase; this allows us to verify the ability of our time stepping method to integrate accurately through these different phases. Parameters V_p and τ^∞ are the plate rate and magnitude of remote stress and are taken to be constant; see Table 1. The parameter δ is the total slip during the coseismic phase, and we take it to be equal to $\delta = (V_p + V_{\min})t_e$, where t_e is the time of the coseismic event and $V_{\min}$ is the minimum slip velocity; see Table 1.

The spatial dependency of the manufactured solution is given by

$$\phi(y,z) = \frac{H(H+y)}{(H+y)^2 + z^2}, \tag{53}$$

where H is a locking depth given in Table 1. When evaluated along the fault (at $y = 0$) ϕ takes the form of a normalized Lorentzian distribution. The temporal dependency of the manufactured solution is

$$K(t) = \frac{1}{\pi}\left[\arctan\left(\frac{t-t_e}{t_w}\right) + \frac{\pi}{2}\right] + \frac{V_{\min}}{\delta}t, \tag{54}$$

and is designed to test the adaptive time-stepping of the numerical scheme. The system is first loaded at the plate rate of V_p, this corresponds to the interseismic period. When the system reaches event time t_e, slip velocity increases over many orders of magnitude, simulating a rupture event with duration t_w. Velocity then returns to its minimum rate, $V_{\min}$, for the rest of the simulation.

The exact solution sets the initial data for differential equations (28a) and (30b) and allows us to solve for the exact shear stress $\hat{\tau}_{qs}$ via (29) and the exact slip velocity $\hat{V}$ via (28). Plugging these into (33) allows us to solve for $\hat{\psi}$, namely

$$\hat{\psi} = a \ln \left[\frac{2V_0}{\hat{V}} \sinh \left(\frac{\hat{\tau}_{qs} - \eta \hat{V}}{\sigma_n a} \right) \right]. \tag{55}$$

The boundary data $g_L(t, z)$ is obtained via integration of the ODEs, as detailed in section 4. Note that as done in Erickson and Dunham (2014), we must add a source term to (30b), i.e. to update state evolution we now numerically integrate

$$\frac{\partial \psi}{\partial t} = G(V, \psi) + \frac{\partial \hat{\psi}}{\partial t} - G(\hat{V}, \hat{\psi}). \tag{56}$$

The manufactured solution we have chosen does not satisfy the traction free boundary condition, and thus we instead enforce the top and bottom stress boundary conditions:

$$\sigma_{xz}(t, y, 0) = \left[\mu_2 \frac{\partial \hat{u}}{\partial y} + \mu_3 \frac{\partial \hat{u}}{\partial z} \right] \bigg|_{z=0}, \quad \sigma_{xz}(t, y, L_z) = \left[\mu_2 \frac{\partial \hat{u}}{\partial y} + \mu_3 \frac{\partial \hat{u}}{\partial z} \right] \bigg|_{z=L_z}. \tag{57a}$$

Similarly, the remote boundary data is defined by the manufactured solution,

$$g_R(t, z) = \hat{u}(t, L_y, z). \tag{58}$$

Because our main focus is to explore the effects of anistotropy within a homogeneous medium, we run convergence tests for both the orthotropic ($\mu_2 = 0$) and fully anisotropic ($\mu_2 \neq 0$) cases with constant coefficients, and verify that the numerical solution converges to the exact solution at the expected rate for a a second-order accurate method. At the end of each simulation, we compute the relative error in the discrete H-norm, given by

$$\text{Error}_H(h) = \frac{\|\hat{\mathbf{u}} - \mathbf{u}\|_H}{\|\hat{\mathbf{u}}\|_H}. \tag{59}$$

All the parameter values used in the convergence test simulations are located in Table 1. Table 2 and Table 3 show the successive relative errors and convergence rates under mesh refinement for the orthotropic and fully anisotropic cases respectively.

Table 1: Parameters used in manufactured solution convergence tests.

Parameter	Definition	Value
L_y	Fault domain length	72 km
L_z	Off-fault domain length	72 km
H	Locking Depth	12 km
μ_1	Material stiffness parameter	36 GPa
μ_2	Material stiffness parameter	variable GPa
μ_3	Material stiffness parameter	variable GPa
ρ	Density	2800 kg/m^3
σ_n	Normal stress in fault	50 MPa
τ^∞	Remote shear stress	31.73 MPa
t_f	Final simulation time	70 years
t_e	Event nucleation time	35 years
t_w	Timescale for event duration	10 s
a	Rate-and-state parameter	0.015
b	Rate-and-state parameter	0.02
D_c	critical slip distance	0.2 m
V_p	Plate rate	10^{-9} m/s
$V_{\min}$	Minimum slip velocity	10^{-12} m/s
V_0	Reference velocity	10^{-6} m/s
f_0	Reference friction coefficient	0.6

Table 2: Relative error for the orthotropic case ($\mu_3 = 24$ GPa, $\mu_2 = 0$ GPa), computed in the discrete $\mathbf{H}$ norm with $N = N_y = N_z$. The rate of convergence approaches 2 under mesh refinement.

N	Error(h)	Rate
2^4+1	2.2541×10^{-2}	–
2^5+1	6.0595×10^{-3}	1.89527880
2^6+1	1.5770×10^{-3}	1.94205097
2^7+1	4.0235×10^{-4}	1.97063645
2^8+1	1.0072×10^{-4}	1.99809893

Table 3: Relative error for the fully anisotropic case ($\mu_2 = 18$ GPa, $\mu_3 = 36$ GPa), computed in the discrete $\mathbf{H}$ norm with $N = N_y = N_z$. The rate of convergence approaches 2 under mesh refinement.

N	Error(h)	Rate
2^4+1	3.3244×10^{-2}	–
2^5+1	8.9966×10^{-3}	1.88564247
2^6+1	2.3099×10^{-3}	1.96151856
2^7+1	5.82×10^{-4}	1.98782444

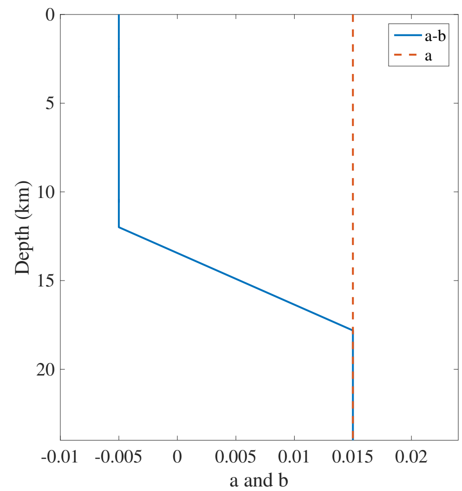

Figure 1: Depth variation of frictional parameters a and b shown down to a depth of 24 km. Below this depth the parameters remain constant, namely $a - b = a = 0.015$.

7 Results of Parameter-varying Study

Here we use the numerical scheme detailed in Section 3 and Section 4 to study earthquake cycles in anisotropic media. We begin by considering an orthotropic media ($\mu_2 = 0$) and conduct a parameter study by varying μ_1 and μ_3 (holding all other parameters fixed). Rate-and-state friction parameters a and b vary with depth, as illustrated in Figure 1. Negative values of $a - b$ correspond to the velocity-weakening (seismogenic) zone where earthquakes occur. At depths for which $a - b$ is positive, below ∼12 km depth, the fault undergoes steady-state sliding. We find that anisotropy influences the periodicity of a simulation, the length of the interseismic period, and that many of the simulations host aseismic transient events. In section Section 7.3 we investigate the relationship between these transients, nucleation zone, and interseismic creep. Due to the large scope of the parameter study, and the complexity of the results, we begin by studying the orthotropic problem and examine some illustrative examples. With the groundwork in place to better understand the entire set of results, we discuss all of our findings in Section 7.4. The entire parameter study is summarized in Table 5. In Section 7.5 we present preliminary results from the study of the fully anisotropic problem, and section Section 7.6 illustrates the effects of anisotropy on surface velocity profiles.

Even though inertial effects are not considered in our simulations, it is useful to consider the waves speeds for an anisotropic medium in order to connect the model parameters with observations. Since the material stiffness matrix $\mathbf{M}_\mu$ is symmetric, positive definite, it can be diagonalized as

$$\mathbf{M}_\mu = \begin{bmatrix} \mu_1 & \mu_2 \\ \mu_2 & \mu_3 \end{bmatrix} = \mathbf{V} \begin{bmatrix} \lambda_1 & 0 \\ 0 & \lambda_2 \end{bmatrix} \mathbf{V}^T, \tag{60}$$

where $\mathbf{V}$ has the orthogonal eigenvectors of $\mathbf{M}_\mu$ as its columns and $\lambda_1,\ \lambda_2 > 0$. This means

Table 4: Parameters used parameter varying study.

Parameter	Definition	Value
L_y	Fault domain length	72 km
L_z	Off-fault domain length	72 or 120 km (see Appendix B)
μ_1	Material stiffness parameter	variable GPa
μ_2	Material stiffness parameter	variable GPa
μ_3	Material stiffness parameter	variable GPa
ρ	Density	2800 kg/m^3
σ_n	Normal stress in fault	50 MPa
τ^∞	Remote shear stress	31.73 MPa
a	Rate-and-state parameter	0.015
b	Rate-and-state parameter	depth variable
D_c	critical slip distance	8 mm
V_p	Plate rate	10^{-9} m/s
V_0	Reference velocity	10^{-6} m/s
f_0	Reference friction coefficient	0.6

that the orthogonally split shear waves have fast and slow wave speeds

$$c_{\text{fast}} = \sqrt{\frac{\max\{\lambda_1, \lambda_2\}}{\rho}}, \tag{61a}$$

$$c_{\text{slow}} = \sqrt{\frac{\min\{\lambda_1, \lambda_2\}}{\rho}}. \tag{61b}$$

The fast wave travels in the direction of the eigenvector associated with the maximum eigenvalue and the slow wave travels in the direction of the eigenvector associated with the minimum eigenvalue.

Anisotropy measurements from shear wave splitting techniques used following the M7.1 Hector Mine earthquake (which occurred along a strike-slip fault) find anisotropy confined to the upper 2-3 km depth of the fault, with average fast directions oriented between fault parallel (within the horizontal plane) and parallel to the direction of regional maximum compressive stress (Cochran et al., 2003). Fast direction oriented with the fault-perpendicular direction, however, have also been observed (Stuart et al., 2002). Cochran et al. (2003) compute an apparent crack density $\epsilon = v_s \delta t/L$, where v_s is the fast shear wave velocity, and $\delta t/L$ is a path-normalized delay time between arrivals of the fast and slow shear waves, and report values of ϵ to be approximately 5%, and generally less than 10%, regardless of region. Thus the relationship between wave speeds is

$$c_{slow}(1 + \epsilon) = c_{fast}, \tag{62}$$

which translates to a relationship between shear moduli given by

$$\max\{\lambda_1, \lambda_2\}/\min\{\lambda_1, \lambda_2\} = (1 + \epsilon)^2. \tag{63}$$

A maximum value of ϵ of 10% corresponds to an approximate 20% difference in shear moduli. We consider parameter values both within and outside this range in order to explore the full range of possible effects of anisotropy on the earthquake cycle.

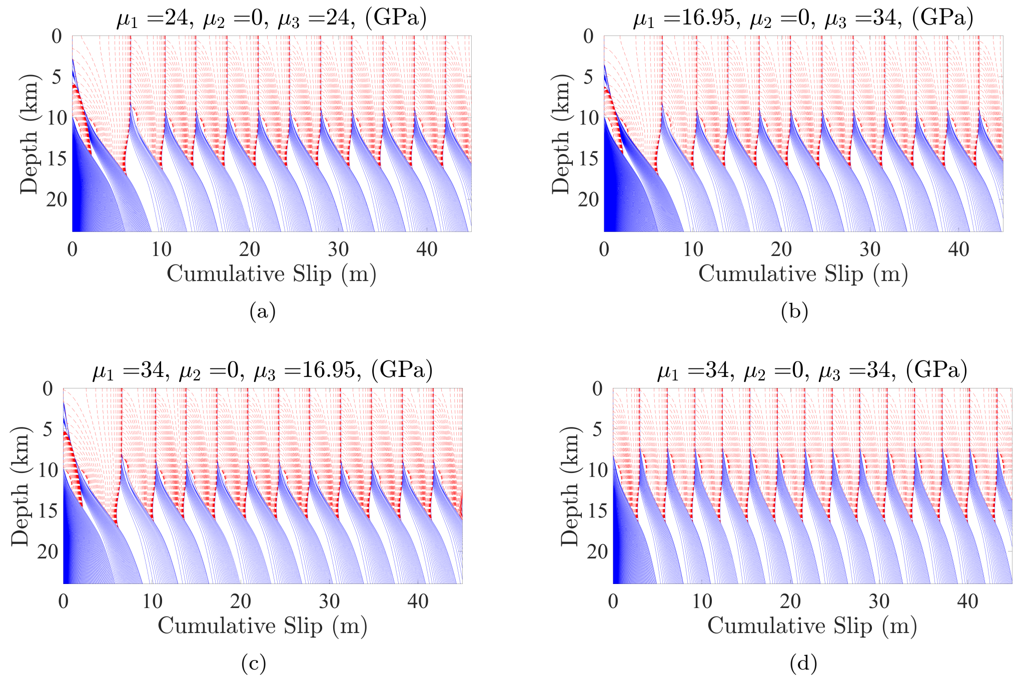

Figure 2: Cumulative slip plotted in blue every 5-a during the interseismic periods, and in red every second during quasi-dynamic rupture for (a) an HTI simulation with $\mu_1 = 34$ GPa, $\mu_3 = 16.95$ GPa, (b) a VTI simulation with $\mu_1 = 16.95$ GPa, $\mu_3 = 34$ GPa, (c) an isotropic reference with $\mu^* = 24$ GPa, and (d) an isotropic reference case with $\mu_1 = \mu_3 = 34$ GPa.

7.1 Orthotropic anisotropy

For orthotropic anisotropy ($\mu_2 = 0$), two orthogonally split shear waves travel in either the fault-perpendicular (y-) or fault-parallel (z-) directions. If $\mu_1 > \mu_3$, the material is called horizontal transversely isotropic (HTI) and the fast wave travels in the fault perpendicular direction. When $\mu_1 < \mu_3$ the material is called vertical transversely isotropic (VTI) and the fast wave travels in the fault parallel direction.

For the orthotropic problem we first examined the effects of anisotropy by holding μ_1 constant and decreasing μ_3 (or vice-versa). This corresponds to increasing the degree of HTI or VTI anisotropy. For a related isotropic problem, we consider several cases. One possibility is to choose the isotropic shear modulus, μ, to be either μ_1 or μ_3. An alternative isotropic reference case would be for a given to choose $\mu = \mu^* = \sqrt{\mu_1 \mu_3}$. In the text that follows, each of these choice will be used as relevant to the discussion.

7.2 Simulation results

We first illustrate our findings in Figure 2, where we show results for both an HTI and VTI simulation with $\mu^* = 24$ GPa, along with two isotropic reference cases. In these snapshots, slip is plotted over a sequence of earthquakes spanning about 1500 years, where contours in blue represent the interseimic period, when the maximum slip rate (taken over the fault) is less than 1 mm/s. Slip is plotted in red contours every second during a quasi-dynamic event, when the

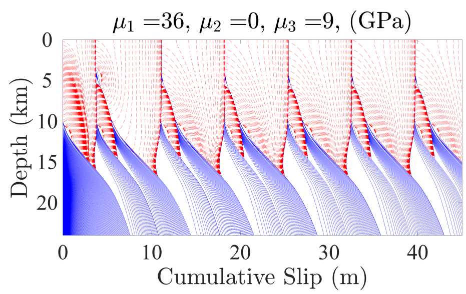

(a)

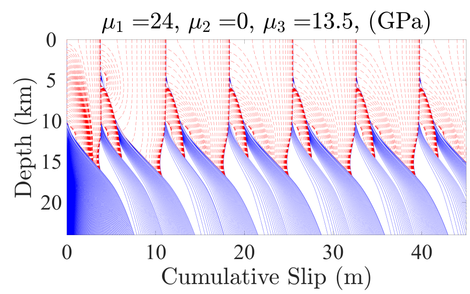

(b)

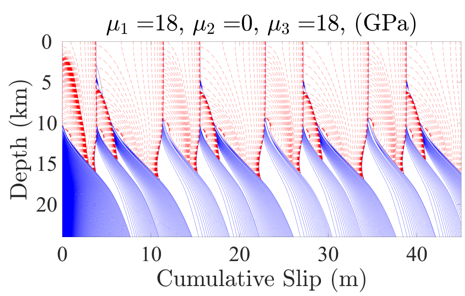

(c)

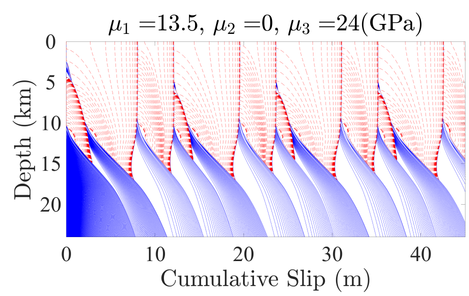

(d)

Figure 3: Cumulative slip plotted in blue every 5-a during the interseismic periods, and in red every second during quasi-dynamic rupture for (a) an HTI simulation with $\mu_1 = 24$ GPa, $\mu_3 = 13.5$ GPa, (b) a second HTI simulation with $\mu_1 = 36$ GPa, $\mu_3 = 9$ GPa, (c) a VTI simulation with $\mu_1 = 13.5$ GPa, $\mu_3 = 24$ GPa and (d) an isotropic reference case with $\mu_1 = \mu_3 = 18$ GPa.

maximum slip rate is greater than 1 mm/s. Figure 2(a) is the HTI simulation, with $\mu_1 = 34$ GPa and $\mu_3 = 16.95$ GPa. Figure 2(b) shows the VTI simulation, where $\mu_1 = 16.95$ GPa and $\mu_3 = 34$ GPa. Figure 2(c) corresponds to an isotropic reference case, where $\mu_1 = \mu_3 = 24$ GPa (to ensure that $\mu^* = 24$ GPa as in each of the anisotropic simulations). Figure 2(d) is the isotropic reference case for which $\mu_1 = \mu_3 = 34$ GPa. Comparing the snapshots of cumulative slip for the first three simulations, we see that they appear qualitatively similar. After a spin-up period, periodic events nucleate at a depth of approximately 10 km, and accumulate $\sim$3.5 m of slip at Earth's surface. Comparing these to Figure 2(d), where events nucleate further updip, and accumulate only $\sim$3 m slip with each event, we note that a decrease in either μ_1 or μ_3 (or both) increases the recurrence interval and thus the amount of slip during each earthquake. These results suggest that μ^*, rather than absolute values of μ_1 and μ_3 determine model outcomes, including recurrence interval and nucleation depth.

Since results remain similar for all cases with $\mu^* = 24$ GPa, we hypothesize that μ^* predominantly determines emergent behavior. To explore this, Figure 3 presents several cases with $\mu^* = 18$ GPa and differing combinations of μ_1 and μ_3. Here we have an alternating sequence of large and small events nucleate at a depth of $\sim$12 km, a result seen by Lapusta and Rice (2003) for a decrease in h^* (obtained by reducing the value of D_c rather than in shear modulus). This behavior persists with stronger HTI anisotropy as seen in Figure 3(a), with $\mu_1 = 36$ GPa and $\mu_3 = 9$ GPa. Interestingly, however, with the anisotropy reversed, the VTI simulation with $\mu_1 = 13.5$ GPa and $\mu_3 = 24$ GPa exhibits a more complex sequence of large, small, and medium sized events, as seen in Figure 3(d). This VTI simulation compares most closely with the isotropic reference case corresponding to $\mu^* = 18$ GPa, as seen in Figure 3(c). Comparing all results shown in Figure 3 we observe that similar μ^* values can generate quite different behaviors. We refer to these different types of behaviors as period two (in which large and small events emerge) and period three (where small, large, and medium sized events emerge).

7.3 Aseismic Transients

In this parameter study we find that many simulations host transient events, where small increases in maximum slip rate emerge between large events. Aseismic transients are observed in other numerical simulations of earthquake sequences and are of interest to the broader community because they might indicate an impending large event (Lapusta and Liu, 2009; Noda, Nakatani, et al., 2013; Noda and Hori, 2014).

In a study of transient events that emerge in earthquake cycle simulations within an isotropic medium, Noda and Hori (2014) find that A/B is a significant parameter that controls interseismic behavior within a seismogenic patch, where $A = a\sigma_n$ is the direct effect and $B = b\sigma_n$ is the evolution effect in the rate-and-state friction law. They deduce that for $A/B \geq 0.6$, aseismic transients events emerge when creep penetrates sufficiently far enough into the velocity-weakening zone to violate linear stability, a length scale given by h^*, but before the creeping region can accommodate dynamic rupture, a length scale referred to as the nucleation size, which scales directly with the shear modulus μ. If we interpret this length scale for our anisotropic problems to scale with μ^* we can contextualize our results in terms of these findings.

In our simulations the rate-and-state parameters a and b and the normal stress σ_n are fixed for all simulations. Thus A and B are fixed, with $A/B = 0.75$ within the seismogenic zone. We define an aseismic transient as an event where the maximum slip velocity (taken over the whole fault) climbs above a threshold of 10^{-9}m/s but remains below the threshold of 1 mm/s (which we define to be the threshold for coseismic speeds). In Figure 4(a) we plot the time series of maximum slip velocity for the simulations from Figure 2. The first three simulations from Figure 2 share the same μ^* value and have close to identical recurrence intervals of

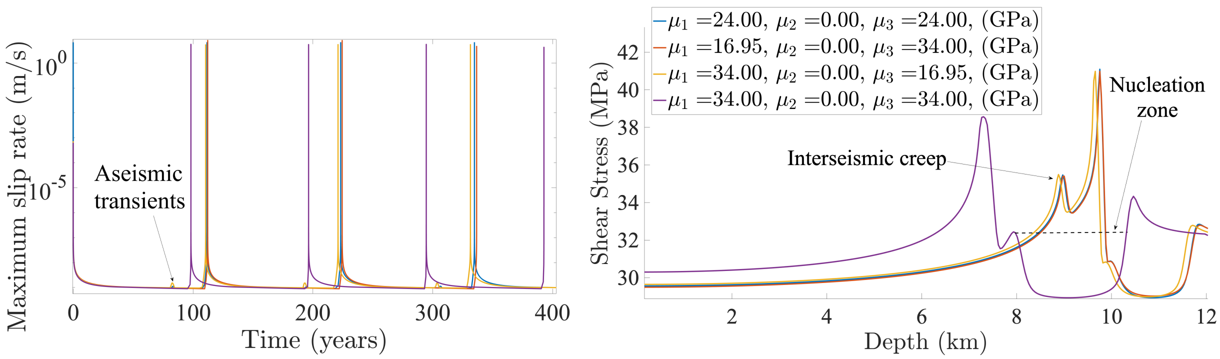

(a) (b)

Figure 4: (a) Maximum slip velocity time series and (b) fault shear stress plotted against depth for simulations from Figure 2 with $\mu^* = 24$ GPa.

about 110 years, but have some subtle differences. We observe that the HTI case (yellow) and the isotropic reference case (blue) both host aseismic transients, where small increases in maximum slip velocity occur approximately 20 years before each large event. The VTI case with the same μ^* value (red), however, does not host transients. In Figure 4(b) we plot the nucleation zones for the simulations in Figure 2, where fault shear stress is plotted as function of depth at the moment when rupture accelerates to coseismic speeds. The nucleation zone width we approximate numerically by computing the distance between the stress peaks surrounding the accelerating slip patch as in Rubin and Ampuero (2005). Smaller peaks further up-dip correspond to where interseismic creep has penetrated into the velocity weakening zone. The first three simulations from Figure 2 all have the same μ^*, and thus the same values of h^* and nucleation size. And yet aseismic transients exist for only two of the simulations. For these simulations we observe that interseismic creep penetrates further up-dip for larger ratios $R = \mu_1/\mu_3$, before nucleation takes place, and numerical measurements show quite similar nucleation lengths of $\sim$2 km; see Figure 4(b). The isotropic reference case in purple (with a larger μ^*) nucleates higher up-dip and has a nucleation length of $\sim$3 km.

Figure 5 shows the time series of maximum slip velocity, and the nucleation zones for all four simulations from Figure 3. In Figure 5(a), we observe that all four simulations host aseismic transients. The HTI simulations (blue and red) each host an aseismic transient before a large event, while the isotropic reference case with the same μ^* (yellow) and the VTI case (purple) host transients before medium events. Examining the recurrence of events we see that for the HTI simulations, the interval before a large event is $\sim$161 years, and $\sim$65 years before a small event. The isotropic reference and VTI simulations, on the other hand, show some differences. The interval before a small event in the period three cycle, is $\sim$84 years for both simulations. However, the interval before medium and large events differs for these two simulations: $\sim$106 and $\sim$178 years, respectively, for the isotropic reference but only $\sim$96 and $\sim$184 years (respectively) for the VTI case. We note that since the isotropic reference case hosts larger aseismic transients than the VTI, the difference in recurrence times between events may be due to this feature. Figure 5(b) shows fault shear stress plotted against fault depth at the moment that maximum velocity reaches the threshold for coseismic slip. Residual stress from small sub-surface events lingers at $\sim$5 km depth for all simulations. In addition, between $\sim$5 and $\sim$6 km depth we see a spike in shear stress leftover from the aseismic transient - we refer to in the figure as a failed rupture, or rupture that failed to reach coseismic speeds.

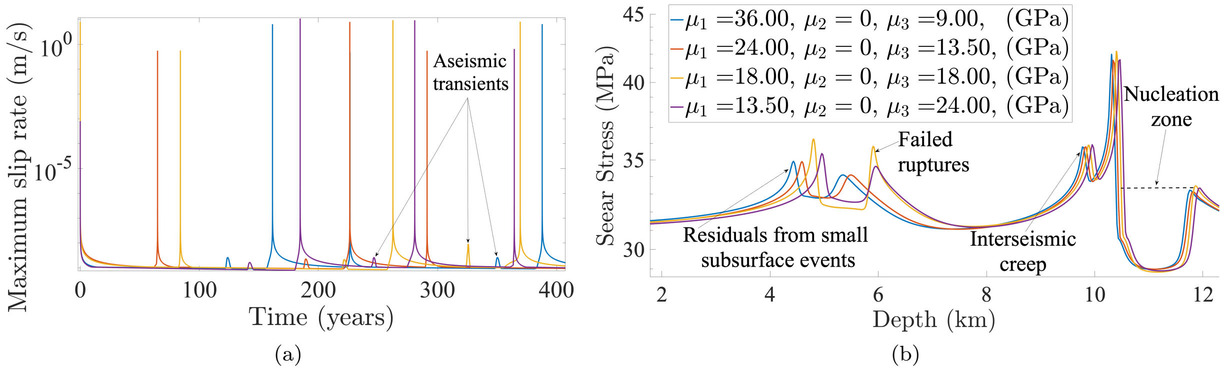

Figure 5: (a) Maximum slip velocity time series and (b) fault shear stress plotted against depth for simulations from Figure 3 with $\mu^* = 18$ GPa.

Just as in Figure 4(b), larger ratios $R = \mu_1/\mu_3$ correspond to interseismic creep penetration further up-dip. Nucleation zone length and location is quite similar for all events, with length of ∼1.4 km, and location between ∼10 and ∼12 km depth. In this parameter regime, therefore, the emergence of aseismic transients cannot be attributed solely to A, B and μ^*. The ratio R seems to determine how far creep penetrates up-dip before nucleation takes. The results we've presented thus far begin to reveal a more complex relationship between R, the nucleation zone, the presence of transients, and interseismic creep penetration. However, it is challenging to isolate the influence of any one of these factors.

7.4 Periodicity in parameter space

To better understand what determines period one, two or three behaviors, like those evidenced in Figures 2-3, we conducted a broad sweep of parameter values and list the results in Table 5. Descending the rows of Table 5 correspond to an increase in μ_1, while moving left to right corresponds to increasing values of μ_3. The value in the interior of each cell is the corresponding value of μ^*. The colors of each cell correspond to the period of the simulation. Yellow indicates that the simulation has period one, red indicates period two, and blue indicates period three. Simulations with the same μ^* value, for which differences in period occur when μ_1 and μ_3 are varied, are circled to highlight these differences. For example simulations with $(\mu_1, \mu_3) = (30, 15)$ (row 12, column 4) and $(15, 30)$ (row 4, column 12) share a μ^* value of 21.21 but are period three and period one respectively. Similarly, $\mu^* = 18$ for simulations $(\mu_1, \mu_3) = (24, 13.5)$ and $(18, 18)$, but $(\mu_1, \mu_3) = (24, 13.5)$ is period two while $(\mu_1, \mu_3) = (18, 18)$ is period three. Bold cell value denote that the simulation hosts aseismic transients. White cells are simulations that are outside of the scope of this parameter study.

Table 5 reveals a bifurcation from period one to period two behavior by decreasing μ^*, with a complex boundary between regimes where period 3 behavior emerges. The circles reveal that simulations with the same μ^* can have quite different behaviors and periodicity, and the transition from italicized to bold fonts reveal that for most parameter values, a decrease in μ^* corresponds to a transition from period one, to period one with aseismic transients, to period three with no aseismic transients, to period three with aseismic transients, to period two.

To ascertain more about the relationship between the ratio $R = \mu_1/\mu_3$, nucleation zone, and aseismic transients, we examine column 10 of Table 5, that is the column where $\mu_3 = 24$.

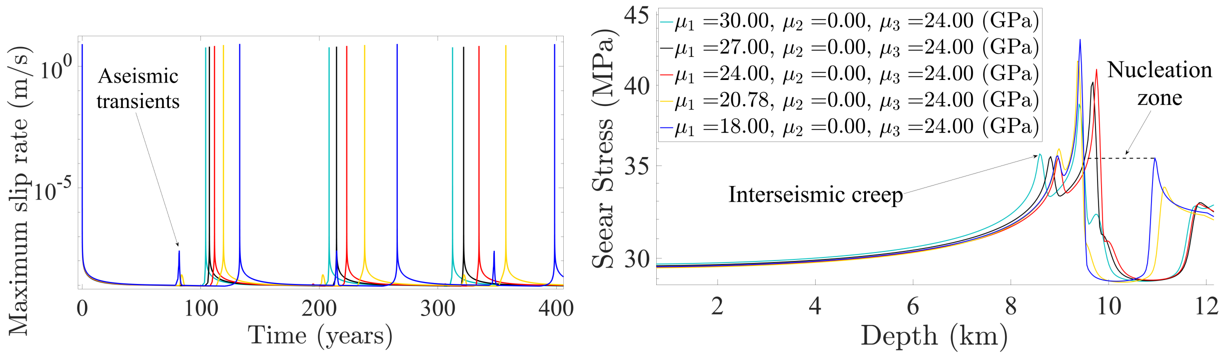

(a) (b)

Figure 6: Maximum slip velocity and fault shear stress profiles shown for a representative sample of the simulations in Table 5 where μ_1 is allowed to vary and μ_3 is held constant at 24 GPa.

Note that to explore the role of R without having to vary both μ_1 and μ_3 at once (which further complicates analysis), it is necessary to instead vary μ^*. In Figure 6 we present the maximum slip velocity time series, and nucleation zones for a representative subset of the period one simulations from column 10, with a range of ratios of μ_1/μ_3. Based on the results presented thus far, we expect μ_1 to dictate how far up-dip interseismic creep is able to penetrate. As such, we would expect the extent of creep to be farthest up-dip for the highest ratio of R (shown in teal for $R = 1.25$) and lowest for the smallest ratio (shown in blue for $R = 0.75$). However, this is not entirely the case. Although the $R = 0.75$ case has the smallest nucleation zone and the smallest μ_1, interseismic creep is able to penetrate further up than the cases shown in red and yellow. Moreover, creep penetrates about as far up-dip for with larger μ_1/μ_3 ratios, namely, the red and yellow curves corresponding o $R = 1$ and $R =\approx 0.87$, respectively. We attribute this to the influence of the interseismic transients present in both the $R = 1$ (yellow) and $R = 0.75$ (blue) simulations, (as evidenced in Figure 6(a)). These results suggest that while R seems to govern nucleation zone size, and largely dictates how far up-dip interseismic creep can penetrate, the presence and magnitude of aseismic transients also plays a role.

To further explore aseismic transients events in other parts of parameter space, we looked more closely at some results from Table 5. In Figure 7 we present plots of slip profiles for four simulations where μ_1 or μ_3 is set to 20.78 GPa and the other parameter takes on the values 11.972 GPa or 13.5 GPa. Figures 7(a) and 7(b) show a VTI and an HTI simulation corresponding to $\mu^* = 15.77$ GPa. For these parameter values, the same μ^* can generate quite different results. Both simulations generate sequences of large and small events, but the large events in the VTI simulation have a longer recurrence interval, with more slip occurring with each event. Figures 7(c) and 7(d), however, show a VTI and an HTI simulation both with $\mu^* = 16.75$ GPa, where qualitatively similar sequences of events are generated. Figures 7(a) and 7(d) can be used to observe the effect of increasing μ_1, while keeping μ_3 fixed, while Figures 7(b) and 7(c) can be used to observe the effect of fixing μ_1 and varying μ_3.

In Figure 8 the maximum slip velocity time series of all four simulations from Figure 7 is plotted over a period of 350 years. We see that all but one of the simulations hosts aseismic transients. The VTI simulation (in red) with $\mu_1 = 20.78$ GPa, $\mu_3 = 11.97$ GPa doesn't host aseismic transients, while its HTI counterpart (shown in yellow) does. We examine the role of shear stress in more detail in Figure 8(b), where the nucleation zones are shown for all four simulations. Higher ratios of μ_1/μ_3 again correspond to further penetration up-dip of

Table 5: μ_1 values are located in the first column, while μ_3 values are in the first row. The interior cells contain the μ^* value that corresponds to each μ_1, μ_3 pair. Color indicates the period of a simulation, yellow is period one, red is period two, and blue is period three. Bold font denotes a simulation that hosts aseismic transients. Circled cells are simulations for which a period change occurs for parameter-differences in simulations with the same μ^* value.

μ_1 \ μ_3	**9**	**11.972**	**13.5**	**15**	**16.95**	**18**	**19.39**	**20.78**	**22**	**24**	**27**	**30**	**36**
9	9.00	10.38	11.02	11.62	12.35	**12.73**	13.21	**13.68**	**14.07**	**14.70**	**15.59**	**16.43**	**18.00**
11.972	10.38	11.97	12.71	13.40	**14.25**	**14.68**	**15.24**	**15.77**	**16.23**	**16.95**	**17.98**	18.95	**20.76**
13.5	11.02	12.71	13.50	14.23	15.13	**15.59**	**16.18**	**16.75**	**17.23**	**18.00**	19.09	20.12	**22.05**
15	11.62	13.40	14.23	15.00	**15.95**	**16.43**	**17.05**	**17.66**	**18.17**	18.97	20.12	**21.21**	23.24
16.95	12.35	14.25	15.13	**15.95**	**16.95**	**17.47**	**18.13**	18.77	19.31	20.17	**21.39**	**22.55**	24.70
18	**12.73**	14.68	15.59	**16.43**	**17.47**	**18.00**	**18.68**	19.34	19.90	**20.78**	**22.05**	**23.24**	25.46
19.39	13.21	15.24	**16.18**	**17.05**	**18.13**	**18.68**	19.39	20.07	20.65	**21.57**	**22.88**	24.12	26.42
20.78	13.68	15.77	**16.75**	**17.66**	**18.77**	19.34	20.07	20.78	**21.38**	**22.33**	23.69	24.97	27.35
22	14.07	16.23	**17.23**	**18.17**	19.31	19.90	20.65	**21.38**	**22.00**	**22.98**	24.37	25.69	28.14
24	14.70	**16.95**	**18.00**	**18.97**	20.17	20.78	**21.57**	**22.33**	**22.98**	24.00	25.46	26.83	29.39
27	15.59	**17.98**	**19.09**	20.12	21.39	**22.05**	**22.88**	**23.69**	24.37	25.46	27.00	28.46	31.18
30	16.43	**18.95**	20.12	21.21	**22.55**	**23.24**	**24.12**	**24.97**	25.69	26.83	28.46	30.00	32.86
36	**18.00**	20.76	**22.05**	**23.24**	**24.70**	25.46	26.42	27.35	28.14	29.39	31.18	32.86	36.00

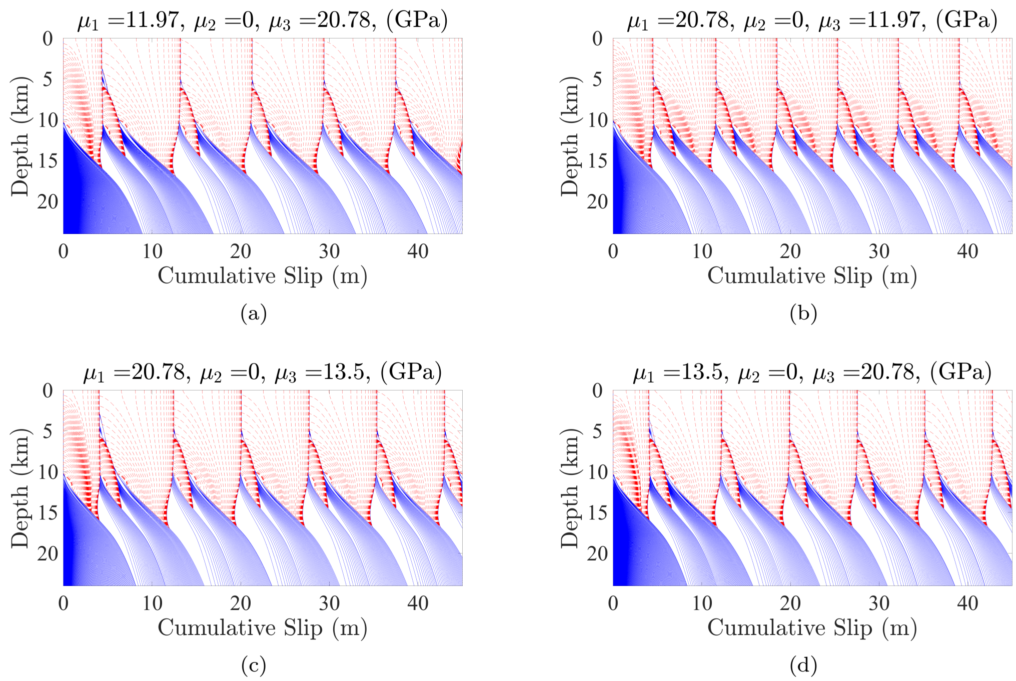

Figure 7: Cumulative slip plotted in blue every 5-a during the interseismic periods, and in red every second during quasi-dynamic rupture for (a) a VTI simulation with $\mu_1 = 11.97$ GPa, $\mu_3 = 20.78$ GPa, (b) an HTI simulation with $\mu_1 = 20.78$ GPa, $\mu_3 = 11.97$ GPa, (c) an HTI simulation with $\mu_1 = 20.78$ GPa, $\mu_3 = 13.5$ GPa and (d) a VTI simulation with $\mu_1 = 13.5$ GPa and $\mu_3 = 20.78$ GPa.

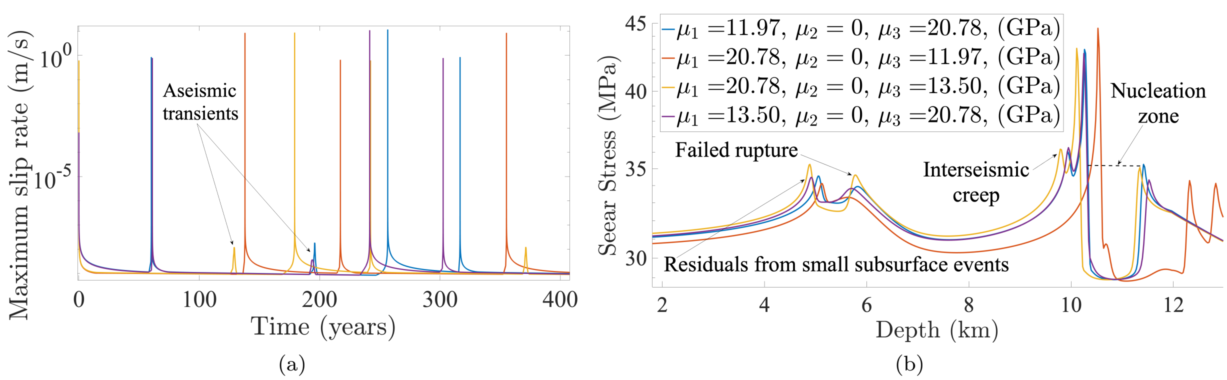

Figure 8: (a) Maximum slip velocity and (b) fault shear stress plotted against depth shows nucleation zones for simulations from Figure 7.

the interseismic creeping region, but does not correspond to whether or not transient events emerge, complicating the explanation given for transient presence and magnitude for the results in Figure 7.

7.5 Full Anisotropy

As a final study, we report on some results when considering full anisotropy, i.e. where $\mu_2 \neq 0$. Figure 9 shows results for both $\mu^* = 24$ GPa and 18 GPa, which can be compared to the orthotropic results with similar μ^* in Figures 2 and 3. We found that these simulations required quite long spin-up periods, thus we plot cumulative slip profiles here relative to a background slip profile, so that figures may be more easily visualized. That is, we plot slip profiles relative to the total slip accumulated during the spin-up period.

Figure 9(a) shows results for $(\mu_1, \mu_2, \mu_3) = (18.39, 7, 34)$ GPa, corresponding to a fast wave direction of about 20 degrees from fault parallel (within the vertical plane) which we will refer to as "near-VTI". Figure 9(b) is the reverse of this orientation (34, 7, 18.39) with a fast wave speed 20 degrees from fault perpendicular, which we will refer to as "near-HTI". Both cases provide additional evidence that model behaviors with $\mu^* = 24$ GPa are qualitatively similar, despite differences in μ_1, μ_2 and μ_3. However, this result does not persist for other values of μ^*. Figure 9(c) shows results for a near-VTI simulation with $\mu^* = 18$ GPa, with $(\mu_1, \mu_2, \mu_3) = (14.56, 5, 24)$, and a fast-wave direction again about 20 degrees from fault-parallel. Results are qualitatively similar to the VTI simulation shown in Figure 3(d), where small, medium, and large events emerge. Figure 9(d) shows results for an orientation reverse with $(\mu_1, \mu_2, \mu_3) = (24, 5, 14.56)$, with results more similar to the HTI simulation shown in Figure 3(b) where only large and small events emerge.

In Figure 10 we examine the maximum slip velocity time series and nucleation zone profiles for simulations in Figure 9. The near-HTI simulations (red and purple curves) as well as the one with near-VTI (yellow) all host transients, whereas the near-VTI simulation in blue does not. The near-VTI simulation in yellow hosts three transients: one in the recurrence interval leading up to a small event and two more in the recurrence interval preceding a large event. In the latter interval a smaller transient occurs $\sim$38 years before a large event, and then another much larger in magnitude transient occurs $\sim$8 years before a large event. In figure 10(b) we see that the large transient corresponds to a failed event that was able to partially propagate up and down the fault, destabilizing the patch of the fault between $\sim$3.3 and 7.3 km depth, but was unable to nucleate to coeseismic speeds. We suspect the large event corresponding to the near-VTI simulation (in yellow) successfully nucleates further up-dip than the large event in the near-HTI simulation (in purple, a simulation with the same μ^*) as a result of the residual stress from the large aseismic transient $\sim$8 years prior. These results complicate our findings in the orthotropic parameter study, where we observed that transients appear to allow creep to penetrate further up-dip. For this fully anisotropic parameter regime, it appears as though transients allow nucleation to occur in the presence of less up-dip creep. These seemingly conflicting results may be reconciled if we allow for the possibility that the timing within the interseismic period of an aseismic transient also plays a role. As such, the temporal location of aseismic transients should be investigated further in future work.

7.6 Surface Velocity Profiles

In this section we report on surface velocity profiles which could be linked to observables measured at Earth's surface across a fault. Figure 11 shows plots of surface velocity as a function of off-fault distance (y) for the results shown so far. Panels (a)-(c) correspond to orthotropic scenarios and (d) (and corresponding zoom in (e)) shows surface velocities for the

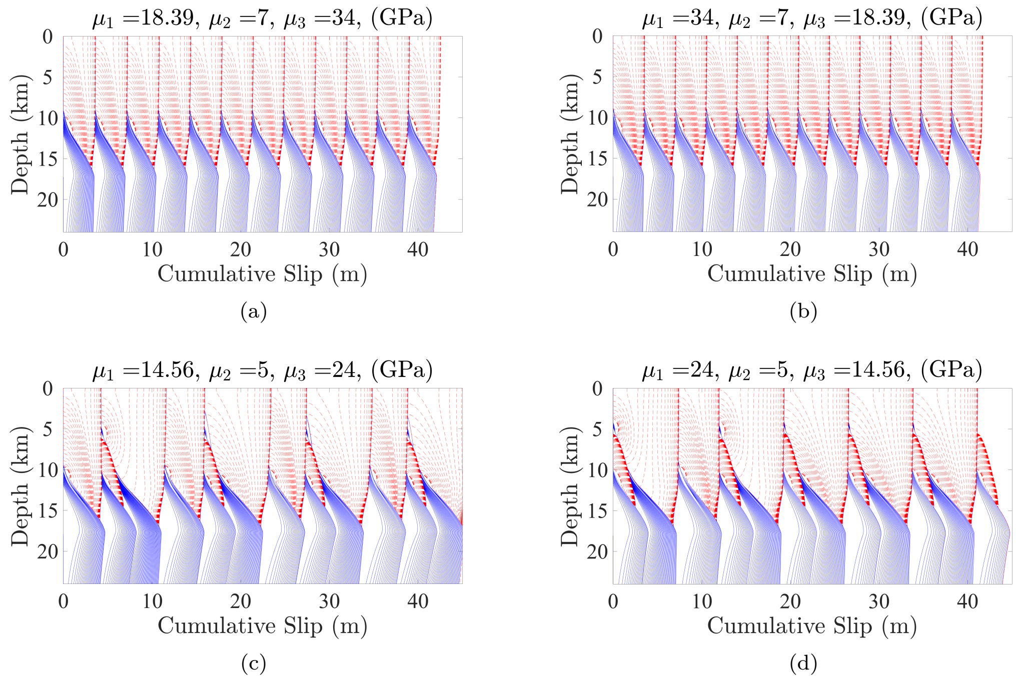

Figure 9: Cumulative slip plotted in blue every 5-a during the interseismic periods, and in red every second during quasi-dynamic rupture for fully anisotropic simulations. In (a) and (b) $\mu^* = 24$, while in (c) and (d) $\mu^* = 18$ GPa. All simulations are plotted relative to a background slip profile.

fully anisotropic scenarios. Dashed and solid contours correspond respectively to 25% and 95% through the recurrence interval preceding a large event for each simulation. Figure 11(a) shows the three similar sequences corresponding to the same μ^* value (blue, red, yellow). In both time instances, the recurrence interval we observe an increase in strain ($\partial u/\partial y$) corresponding to a decrease in μ_1, which is to be expected if shear stress is to remain constant. Strain increases with decreasing μ_1 also for the cases shown in (b)-(c). For the fully anisotropic simulations (d) and zoom (e), this feature persists when comparing those simulations with equivalent μ^*. We include the zoom (e) to illustrate the full anisotropy can allow for small amounts of surface creep during the interseismic period, due to the fact that the $\partial u/\partial z$ component of strain is non-negligible and contributes to the fault shear stress.

8 Discussion and Future Work

We have extended the computational framework developed in Erickson and Dunham (2014) and adapted it to study earthquake cycles in anisotropic media. The off-fault volume is discretized with finite difference operators satisfying a summation-by-parts rule, with weak enforcement of boundary conditions, which leads to a provably stable formulation. Rate-and-state friction is enforced along the fault, and sequences of earthquakes are generated by displacing the remote boundary at a slow plate rate. We tested our numerical scheme by applying it to a suitable manufactured solution and ensuring it achieved the expected order of convergence.

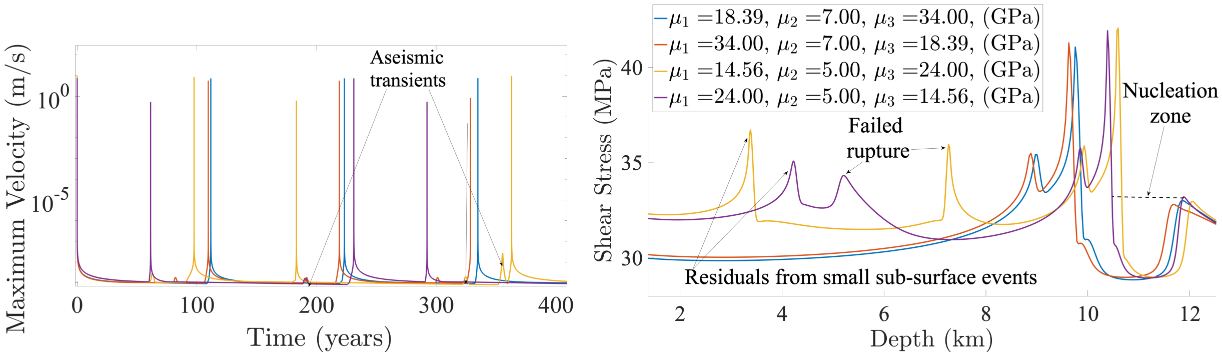

(a) (b)

Figure 10: (a) Maximum slip velocity and (b) fault shear stress plotted against depth shows nucleation zones for simulations from Figure 9 with full anisotropy.

We note that in developing the method for the 2D antiplane problem, we have inherently limited the possible directions for wave-propagation. In fully anisotropic simulations, like the ones in Section 7.5, waves propagate at oblique angles to the fault which cannot be reliably observed in practice. However, real-world observations of fault parallel fast waves, like those in the VTI simulations above, have been made (Stuart et al., 2002).

In the parameter studies in this work, we found that anisotropy influences the recurrence interval, periodicity, emergence of transients, nucleation zone size and depth, and extent of interseimic creep penetration. We found that choices for μ_1/μ_3 can cause simulations with the same μ^* value to exhibit quite different behavior, and uncovered a complex boundary between the period one and period two solutions that naturally arise as one decreases h^*. We found that this boundary often exhibits period three behavior and gives rise to simulations that host aseismic transients. We additionally found that in period two and three solutions, residual stresses from subsurface events appear, and for some simulations failed rupture often occurs near these residual stresses ahead of a coseismic event.

Our results suggest the size and location of the nucleation zone for a simulation, is influenced not just by the ratio μ_1/μ_3, but also by the presence and magnitude of aseismic transients. This suggest that both play a role in how far updip interseismic creep may penetrate. However, the emergence of more complicated aseismic transients in the fully ansiotropic simulations leaves questions to be explored about the relevance of the temporal location of these transients. Additionally, relationships and interactions between the residual stresses from sub-surface events, failed ruptures near these, and aseismic transients, should be explored with furthur studies.

Acknowledgments: MBM and BAE were supported through the NSF under Award No. EAR-1547603 and by the Southern California Earthquake Center. SCEC is funded by NSF Cooperative Agreement EAR-0529922 and USGS Cooperative Agreement 07HQAG0008 (SCEC contribution number xxx). JEK was supported under NSF Award No. EAR-1547596. Thanks to Elizabeth Cochran for useful discussion.

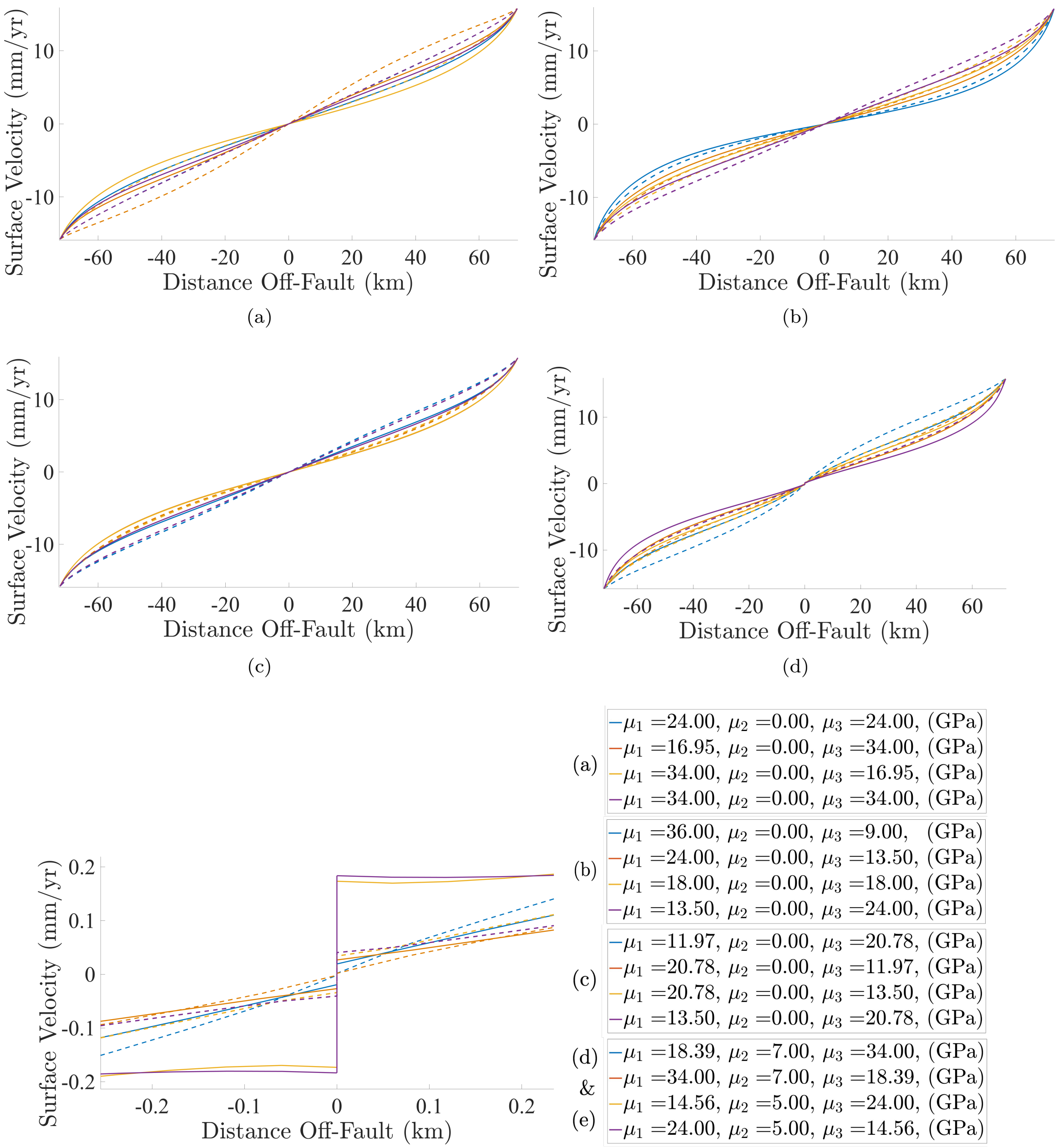

Figure 11: Surface velocity profiles plotted before a large event, after each simulation is out of its spin-up cycle, with dashed lines 25% of the way into the recurrence interval, and solid lines 95% of the way into the recurrence interval. (a)-(c) correspond to the orthotropic simulations from Figures 2-7, while (d) and corresponding zoom (e) correspond to the fully anisotropic simulations shown in Figure 9.

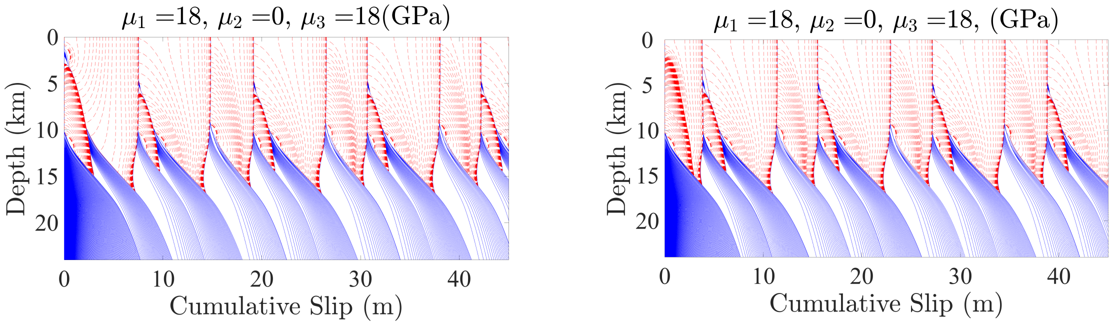

(a) (b)

Figure 12: Cumulative slip plotted in blue every 5-a during the interseismic periods, and in red every second during quasi-dynamic rupture for two, period three, isotropic simulations, where all parameters are held constant. In figure (a) the number of grid points is set to $1,165$ to ensure that cohesive zone L_b is resolved with over 5 grid points, while in figure (b) the grid points are more than doubled to $2,500$ and L_b is resolved with over 10 grid points.

A Appendix: Resolution of the Cohesive Zone

We show our simulations are well-resolved for a period three isotropic problem with $\mu = 18$ GPa . Figure 12 shows cumulative slip profiles, where L_b is resolved with over 5 grid points on the left and over 10 on the right. We see differences only during the spin-up cycle of each simulation, after which both settle into period three behavior that is qualitatively similar.

B Appendix: Choice of Computational Domain

Truncating the off-fault computational domain, L_y, at 72 km causes large events in some of the multi-period simulations in our parameter study to nucleate at an artificially high depth of around 5 km. We suspect that this is due to the influence of finite distance to the remote boundary where loading is enforced. We doubled the domain size for one such simulation, a period two simulation with $\mu_1 = 36$ GPa, and $\mu_3 = 9$ GPa. Increasing the computational domain size leads to large events that nucleate farther down-dip, closer to 12 km depth. In Figure 13 we compare the cumulative slip plots with a domain size of $L_y = 72$ km on the left, and $L_y = 144$ km on the right. It is worth noting that this edge effect, when it occurs, appears in HTI orthotropic simulations where $\mu_1 > \mu_3$, but not in the VTI counterpart (with the same μ^*) for which the values of μ_1 and μ_3 are reversed.

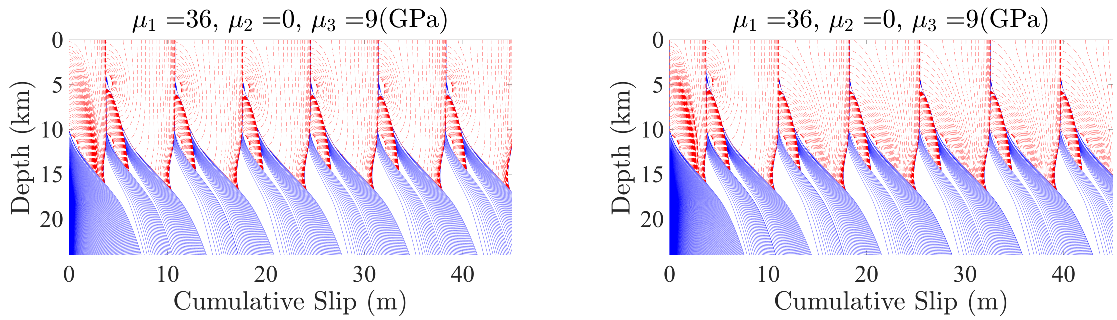

(a)

(b)

Figure 13: Cumulative slip plotted in blue every 5-a during the interseismic periods, and in red every second during quasi-dynamic rupture for two orthotropic simulations with $\mu_1 = 36$ and $\mu_2 = 9$. In figure (a) $L_y = 72$ km. In figure (b) $L_y = 144$ km, i.e. the off-fault computational domain is doubled.

References

Allison, Kali L. and Eric M. Dunham (2018). "Earthquake cycle simulations with rate-and-state friction and power-law viscoelasticity". *Tectonophysics*. Physics of Earthquake Rupture Propagation 733, pp. 232–256. DOI: 10.1016/j.tecto.2017.10.021.

Ampuero, Jean-Paul and Allan M. Rubin (2008). "Earthquake nucleation on rate and state faults Aging and slip laws". *Journal of Geophysical Research: Solid Earth* 113.B1. DOI: 10.1029/2007JB005082.

Cochard, Alain and Raúl Madariaga (1994). "Dynamic faulting under rate-dependent friction". *Pure and Applied Geophysics* 142.3, pp. 419–445. DOI: 10.1007/BF00876049.

Cochran, Elizabeth S., John E. Vidale, and Yong-Gang Li (2003). "Near-fault anisotropy following the Hector Mine earthquake". *Journal of Geophysical Research: Solid Earth* 108.B9. DOI: 10.1029/2002JB002352.

Crampin, Stuart and John H. Lovell (1991). "A decade of shear-wave splitting in the Earth's crust: what does it mean? what use can we make of it? and what should we do next?" *Geophysical Journal International* 107.3, pp. 387–407. DOI: 10.1111/j.1365-246X.1991.tb01401.x.

Dieterich, James H. (1979). "Modeling of rock friction: 1. Experimental results and constitutive equations". en. *Journal of Geophysical Research: Solid Earth* 84.B5, pp. 2161–2168. ISSN: 2156-2202. DOI: 10.1029/JB084iB05p02161.

Erickson, Brittany A. and Eric M. Dunham (2014). "An efficient numerical method for earthquake cycles in heterogeneous media: Alternating subbasin and surface-rupturing events on faults crossing a sedimentary basin". *Journal of Geophysical Research: Solid Earth* 119.4, pp. 3290–3316. DOI: 10.1002/2013JB010614.

Erickson, Brittany A., Eric M. Dunham, and Arash Khosravifar (2017). "A finite difference method for off-fault plasticity throughout the earthquake cycle". *Journal of the Mechanics and Physics of Solids* 109, pp. 50–77. DOI: 10.1016/j.jmps.2017.08.002.

Geubelle, Philippe H. and James R. Rice (1995). "A spectral method for three-dimensional elastodynamic fracture problems". *Journal of the Mechanics and Physics of Solids* 43.11, pp. 1791–1824. DOI: 10.1016/0022-5096(95)00043-I.

Gustafsson, Bertil (1975). "The convergence rate for difference approximations to mixed initial boundary value problems". *Mathematics of Computation* 29.130, pp. 396–406. DOI: 10.1090/S0025-5718-1975-0386296-7.

Hajarolasvadi, Setare and Ahmed E. Elbanna (2017). "A new hybrid numerical scheme for modelling elastodynamics in unbounded media with near-source heterogeneities". *Geophysical Journal International* 211.2, pp. 851–864. DOI: 10.1093/gji/ggx337.

Hicken, J. E. and D. W. Zingg (2013). "Summation-by-parts operators and high-order quadrature". *Journal of Computational and Applied Mathematics* 237.1, pp. 111–125. DOI: 10.1016/j.cam.2012.07.015.

Kaneko, Y., N. Lapusta, and J.-P. Ampuero (2008). "Spectral element modeling of spontaneous earthquake rupture on rate and state faults: Effect of velocity-strengthening friction at shallow depths". *Journal of Geophysical Research: Solid Earth* 113.B9. DOI: 10.1029/2007JB005553.

Kozdon, Jeremy E., Eric M. Dunham, and Jan Nordström (2012). "Interaction of Waves with Frictional Interfaces Using Summation-by-Parts Difference Operators: Weak Enforcement of Nonlinear Boundary Conditions". en. *Journal of Scientific Computing* 50.2, pp. 341–367. ISSN: 1573-7691. DOI: 10.1007/s10915-011-9485-3.

Kreiss, H. -O. and G. Scherer (1974). "Finite Element and Finite Difference Methods for Hyperbolic Partial Differential Equations". *Mathematical Aspects of Finite Elements in Partial Differential Equations*. Ed. by Carl de Boor. Academic Press, pp. 195–212. DOI: 10.1016/B978-0-12-208350-1.50012-1.

Kreiss, H. -O. and G Scherer (1977). "On the Existence of Energy Estimates for Difference Approximations for Hyperbolic Systems".

Lapusta, Nadia and Yi Liu (2009). "Three-dimensional boundary integral modeling of spontaneous earthquake sequences and aseismic slip". *Journal of Geophysical Research: Solid Earth* 114.B9. DOI: 10.1029/2008JB005934.

Lapusta, Nadia and James R. Rice (2003). "Nucleation and early seismic propagation of small and large events in a crustal earthquake model". *Journal of Geophysical Research: Solid Earth* 108.B4. DOI: 10.1029/2001JB000793.

Lapusta, Nadia, James R. Rice, Yehuda BenZion, and Gutuan Zheng (2000). "Elastodynamic analysis for slow tectonic loading with spontaneous rupture episodes on faults with rate- and state-dependent friction". *Journal of Geophysical Research: Solid Earth* 105.B10, pp. 23765–23789. DOI: 10.1029/2000JB900250.

Long, Maureen D. and Thorsten W. Becker (2010). "Mantle dynamics and seismic anisotropy". *Earth and Planetary Science Letters* 297.3, pp. 341–354. DOI: 10.1016/j.epsl.2010.06.036.

Marone, Chris (1998). "Laboratory-Derived Friction Laws and Their Application to Seismic Faulting". *Annual Review of Earth and Planetary Sciences* 26.1, pp. 643–696. DOI: 10.1146/annurev.earth.26.1.643.

Mattsson, Ken and Jan Nordström (2004). "Summation by parts operators for finite difference approximations of second derivatives". *Journal of Computational Physics* 199.2, pp. 503–540. DOI: 10.1016/j.jcp.2004.03.001.

Noda, H., Eric M. Dunham, and James R. Rice (2009). “Earthquake ruptures with thermal weakening and the operation of major faults at low overall stress levels”. *Journal of Geophysical Research: Solid Earth* 114.B7. DOI: 10.1029/2008JB006143.

Noda, H. and T. Hori (2014). “Under what circumstances does a seismogenic patch produce aseismic transients in the later interseismic period?” *Geophysical Research Letters* 41.21, pp. 7477–7484. DOI: 10.1002/2014GL061676.

Noda, Hiroyuki, Masao Nakatani, and Takane Hori (2013). “Large nucleation before large earthquakes is sometimes skipped due to cascade-upImplications from a rate and state simulation of faults with hierarchical asperities”. *Journal of Geophysical Research: Solid Earth* 118.6, pp. 2924–2952. DOI: 10.1002/jgrb.50211.

Ranjith, K. and H. Gao (2007). “Stability of frictional slipping at an anisotropic/isotropic interface”. *International Journal of Solids and Structures* 44.13, pp. 4318–4328. DOI: 10.1016/j.ijsolstr.2006.11.025.

Rice, James R. (1993). “Spatio-temporal complexity of slip on a fault”. *Journal of Geophysical Research: Solid Earth* 98.B6, pp. 9885–9907. DOI: 10.1029/93JB00191.

Roache, Patrick J (1998). *Verification and validation in computational science and engineering*. Albuquerque, NM: Hermosa Publishers.

Rubin, Allen M. and Jean-Paul Ampuero (2005). “Earthquake nucleation on (aging) rate and state faults”. *Journal of Geophysical Research: Solid Earth* 110.B11. DOI: 10.1029/2005JB003686.

Strand, Bo (1994). “Summation by Parts for Finite Difference Approximations for d/dx”. *Journal of Computational Physics* 110.1, pp. 47–67. DOI: 10.1006/jcph.1994.1005.

Stuart, Crampin, Theodora Volti, Sebastien Chastin, Agust Gudmundsson, and Ragnar Stefánsson (2002). “Indication of high pore-fluid pressures in a seismically-active fault zone”. *Geophysical Journal International* 151.2, F1–F5. DOI: 10.1046/j.1365-246X.2002.01830.x.

Virta, Kristoffer and Ken Mattsson (2014). “Acoustic Wave Propagation in Complicated Geometries and Heterogeneous Media”. *Journal of Scientific Computing* 61.1, pp. 90–118. DOI: 10.1007/s10915-014-9817-1.